

Deformation structures in the K06-04 core: insight from a multimethod approach

Internship Report – 20 April 2024
Jop Beunen

Author(s)	Jop Beunen
Title	Deformation structures in the K06-04 core: insight from a multimethod approach
Supervisors	Eva de Boever, Loes Buijze, Jelte Stam (TNO) Frank van Ruitenbeek, Chris Hecker (ITC) André Niemeijer (UU)
Report text	TNO Publiek
Number of pages	66
Number of appendices	1

1 Abstract

Sandstone reservoirs hold potential for storage of CO₂ and hydrogen or for the production of geothermal energy. The mineralogy of fractures in sandstone reservoirs plays an important role, as they can behave as barriers or as conduits to fluid flow and because they might become seismically active. To elaborate on the understanding of this, an extensive research was done on the Slochteren sandstone that was found in the K06-04 core, situated in the North Sea. The mineralogy of this core was determined with a focus on the deformation structures. Multiple techniques were used including optical light microscope, the scanning electron microscope, the cold cathodoluminescence microscope, and short wavelength infrared hyperspectral imaging to provide comprehensive insights into the mineralogy. Each technique offers distinct advantages and limitations, together facilitating a coherent and multi-scale identification of the mineralogical characteristics of both host rock and deformation structures and interpretation of the diagenetic history of the Slochteren sandstone in this well.

Detrital components include quartz, which is the main constituent, varying from 56.4% to 72.4%, lithic grains varying from about 1-5% and minor components of zircons, rutile, muscovite, and lithic fragments, while authigenic minerals primarily consist of clay, between about 4-20% and dolomite between 2-25%, along with minor occurrences of barite and chlorite. These minerals are distributed throughout the matrix and fractures, alongside the presence of bitumen.

Petrography reveals that at least three deformation features were present. These are all associated with grinding and cataclasis. The first deformation feature was associated with ferroan dolomite that fills a fault zone. Iron rich fluids must have migrated upwards from the Carboniferous Coal Measures having an iron content that was significantly larger than the ferroan dolomites that were found in the matrix. This fault zone has almost no porosity, but literature showed that during the injection of CO₂, leakage might take place in reservoirs with carbonate cap rocks by activation of these carbonate faults. The second deformation structure is related to a clay filled fracture that ends at the aforementioned fault. This fracture contains more porosity than the ferroan dolomite filled fault, but still less than the surrounding matrix. These clays have possibly formed during the Cretaceous, but evidence is inconclusive. The third deformation structure that is found is a bitumen filled slender fault zone that is only visible on a minor scale and has millimeter displacement.

2 Contents

Contents

Deformation structures in the K06-04 core: insight from a multimethod approach	1
1 Abstract	2
2 Contents	3
3 Introduction.....	5
4 Background	7
4.1 Geographical Context	7
4.2 Tectonic and Sedimentary Evolution	8
4.2.1 Basement	8
4.2.2 Precambrian.....	8
4.2.3 Cambrian to Devonian - Caledonian Orogeny	8
4.2.4 Devonian to Permian – Variscan/Hercynian Orogeny	9
4.2.5 Permian.....	9
4.2.6 Triassic.....	9
4.2.7 Jurassic.....	10
4.2.8 Cretaceous	10
4.2.9 Tertiary.....	10
5 Data & Methodology.....	12
5.1 Dataset and Samples.....	12
5.1.1 Dataset.....	12
5.1.2 Samples	15
5.2 Methodology.....	17
5.2.1 Petrographic analysis.....	17
5.2.2 Hyperspectral Imaging.....	19
6 Results.....	26
6.1 Petrography	26
6.1.1 Optical Light Microscope and Point Counting.....	26
6.1.2 Scanning Electron Microscope	29
6.1.3 Cathodoluminescence	31
6.2 Hyperspectral analysis.....	33
6.3 Matrix.....	37
6.4 Deformation structures.....	39
7 Discussion.....	41
7.1 Comparison between the techniques.....	41
7.1.1 Thin Section Analysis	41
7.1.2 Scanning Electron Microscope	41
7.1.3 Cathodoluminescence	42
7.1.4 SWIR	42
7.2 Paragenesis.....	45
7.3 Structural analysis.....	46
7.4 Reservoir Quality.....	49

7.5	Recommendations	50
8	Conclusion	52
9	References.....	53
10	Appendix.....	60
10.1	Ferrous Drop.....	63
10.2	Illite crystallinity.....	64
10.3	Illite vs kaolinite	65

3 Introduction

The primary producing horizon in the southern North Sea gas province comprises aeolian sandstone from the Rotliegend Formation, deposited during the Early Permian period (Glennie and Provan, 1990). These Permian Rotliegend sedimentary rocks, that are in the northwest of Europe important reservoir rocks, hold a significant amount of hydrocarbon reserves (Metz et al., 2005). The sandstone reservoirs have a long history of hydrocarbon exploration and production and therefore hold a great potential for carbon and hydrogen storage, but also for the extraction of geothermal energy, as they have relatively well known geological structures, the reservoir quality is good (i.e. the porosity and the permeability of the sandstones are relatively high), they are volumetrically large, the subsurface data is available, and infrastructure is already in place (Eftekhari, 2021; Metz et al., 2005; Rigby and Alsayah, 2023; Vielstädte et al., 2019). Also, near the North Sea, there are many industrial hubs that could be repurposed to incorporate carbon capture technology, and the North Sea region harbors over half of Europe's carbon dioxide storage capacity (Rigby and Alsayah, 2023).

Sandstone reservoirs display a localized reduction in reservoir quality, which can be attributed to many factors, including fractures. These fracture zones are assumed to be controlling factors in the subsurface movement of fluids, including liquids and gases in siliciclastic deposits (Braathen et al., 2009; Nicol et al., 2017). In sedimentary rocks, the existing fault zones can behave as barriers, impeding the fluid flow across the fault plane or as conduits, facilitating the flow along the fault plane (Ligtenberg et al., 2011; Bense and Person, 2006). However, the extent to which faults and fractures are affected by fluid flow is dependent on several factors: fault zone architecture, rock types, fault zone permeability, the relative permeability and fracture density, fracture orientation relative to the fluid flow direction, fracture clustering, fracture fragmentation and its distribution, fracture aperture size and connectivity, fluid properties, and burial history (Kolyukhin et al., 2010; Nicol et al., 2017). The permeability of these fault rocks, which are closely related to the effective stress and temperature conditions, plays a pivotal role across diverse engineering applications, including petroleum engineering, nuclear waste management, natural gas exploration, carbon capture, utilization and storage (CCUS), hydrogen storage and geothermal exploration (Krevor et al., 2023; Petrie et al., 2014; Sperrevik et al., 2002; Sun et al., 2016). Moreover, the properties of faults can vary over (geological) time and, as a result, have an impact on for example the potential to store carbon or hydrogen into specific reservoirs, but also on the extraction of geothermal energy (Bense and Person, 2006; Nicol et al., 2017).

In cases, the faults and fractures present can modify the storage capacity, maximum injection rates and reservoir pressures (Nicol et al. 2017). For example, challenges arise with CO₂ injection because of the buoyancy forces (Shukla et al., 2010). When injecting CO₂ in its supercritical phase (sCO₂), the density disparity between sCO₂ and the in-situ pore fluid can create significant buoyancy forces, potentially leading to upward migration of carbon dioxide molecules from the injection point, forming a plume at the reservoir-caprock interface (Manda et al., 2024; Rigby and Alsayah, 2023). Pressures at the caprock will increase, with increasing plume thickness, with a potential risk of CO₂ leakage to the atmosphere through connected faults and fractures (Angeli et al., 2009). Mitigating the risk of CO₂ migration to the atmosphere or into economically valuable resources (e.g. water aquifers or hydrocarbon reservoirs), requires an understanding of the conditions under which faults and fractures

facilitate fluid flow from the reservoir, the potential for fault reactivation, and the mechanisms by which such reactivation occurs, whether it will be through seismic or aseismic slip (Birkholzer et al., 2015; Nicol et al., 2017). To better understand the fluid flow characteristics of a system within a reservoir, the knowledge of the mechanical properties and the stress condition of the reservoir and the geometry of the fracture networks, both in seismic-scale and micro-scale, is important (Bjørlykke, 2006; Bjørlykke and Høeg, 1997). To accurately describe fracture properties, it is essential to adopt a method that conceptualizes faults and fractures as volumetric entities comprising distinct structural elements with unique physical characteristics and spatial distributions at a specific observation scale (Braathen et al., 2009).

In sandstone reservoirs, comprehending fracture systems are crucial for hydrocarbon exploration and production, as these networks significantly influence fluid flow properties. Understanding fluid flow dynamics and how they interact with the in-situ mineralogy is essential for mitigating risks in geothermal and carbon capture sites. Since differences in mineral compositions may have a great impact on potential fluid-rock interactions, a detailed study of mineral types, spatial distribution and diagenetic evolution of the sediments are indispensable. To minimize the local geological risks associated with faults in the Dutch subsurface, it is important to delve into the fault mineralogy and strength at significant depths. This report therefore aims to incorporate short wavelength infrared (SWIR) hyperspectral analysis, along with co-located microstructural analyses of thin sections to get a better interpretation of the mineralogy of faults and fractures that are present in the K06-04 core from the North Sea. This core was chosen as faults and fractures crosscut this core and because SWIR data of the full core interval of 9 meters was already obtained and available (Robertson et al., 2023). On top of that, the aim is to investigate whether correlations between the techniques can be made to improve on the different ways to obtain mineralogy data from well cores.

4 Background

4.1 Geographical Context

The North Sea, a marginal sea of the Atlantic Ocean, lies in Northwestern Europe, bordered by the Netherlands, the United Kingdom, Norway, Germany, Belgium, and Denmark (Özmaral et al., 2022). It is a sedimentary basin that is located on the north-western European continental shelf and open to the north, where it grades into the Atlantic Shelf basins of western Norway and the Shetland Islands. The basin is connected with the Baltic Sea in the east through the Skagerrak between Denmark and Norway and with the Atlantic Ocean in the south via the English channel (Thomas et al., 2005; Ziegler, 1977).

The focus of this internship is on a core from the K-block of the Netherlands in the North Sea (Figure 1). The K-block is located within the Dutch offshore sector of the Southern North Sea basin. This basin stretches off the coast of the Netherlands and extends into neighboring countries such as the United Kingdom, Belgium, and Germany (Thomas et al., 2005; Ziegler, 1977). The Southern North Sea basin, can be subdivided into multiple subbasins and holds significant hydrocarbon reserves, that are formed during the Permian era (Glennie, 1997, Ziegler, 1977). The K-block is one of the areas within this basin that has been explored for oil and gas resources (NLOG, 2024).

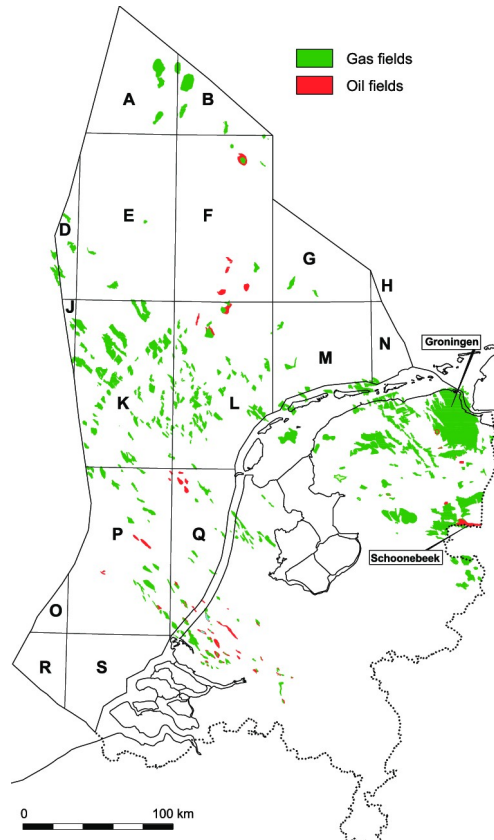


Figure 1: Map of the Netherlands with its hydrocarbon reserves. The K-block is in the North Sea, which is in the Dutch offshore sector. Image from De Jager & Geluk (2007).

4.2 Tectonic and Sedimentary Evolution

The brief history of the evolution of the North Sea Basin is described below. It focuses on the structural and stratigraphic evolution of the area in which the K-block is situated and contains detailed information about predominantly the southern parts of the North Sea Basin.

4.2.1 Basement

In many areas, the upper boundary of the basement lies beyond conventional drilling depths. Consequently, the metamorphic and igneous rocks underlying the North Sea basin have only been reached in a limited number of wells (Ziegler, 1977). On top of this, it is difficult to distinguish between the various rock units or terranes solely based on seismic reflection interpretation, making the identification of the type of crystalline basement rocks difficult (Rosentau et al., 2017). However, the basement rocks have been dated from Caledonian to Precambrian (Ebbing and Olesen, 2010).

4.2.2 Precambrian

The oldest rocks identified in the North Sea basin date back to the Precambrian era and are situated at depth and at the edges of the North Sea Basin. The Precambrian basement rocks are found in regions such as the Ringkobing-Fyn high, as well as in north Jutland, Skagerrak, and the Kattegat, where they extend until the Tornquist Zone (Kent, 1975; Larsen, 1971; Rosentau et al., 2017; Ziegler, 1977). Additionally, Precambrian basement rocks can be found in the Hebrides and in the Scottish Northern Highlands, where they are covered by unmetamorphosed late Precambrian and lower Paleozoic sediments. Further, the Ardennes might be linked to the central North Sea through the southern parts of the North Sea. If so, the Precambrian basement of the London-Brabant massif could be an intramontane stable platform, potentially containing Precambrian basement rocks with lower Paleozoic undeformed sediments (Ziegler, 1977).

4.2.3 Cambrian to Devonian - Caledonian Orogeny

During the Caledonian Orogeny, which took place in the Cambrian to Early Devonian, the collision between the North American-Greenland plate and the Northwest European plate occurred along the Appalachian and Scottish-Norwegian Caledonian Foldbelt. The broad outline of this foldbelt ran from the central North Sea through Germany to Poland, but also in here, only the overall trend can be seen due to scarcity in subsurface data (P. Ziegler, 1975). The foldbelt affected much of the North Sea basin, as the rocks from the Caledonian Orogeny form the second part of the basement rocks (Kent, 1975; P. Ziegler, 1977). A sizable portion of the basement complex of the North Sea basin is formed by the metamorphic and intrusive rocks that can be dated back to this age (Pharaoh et al., 1995). The largest parts of these basement rocks run from Norway all the way through the center of the basin to England, but again, due to scarcity in well data, the boundaries are ill-defined (Pharaoh et al., 1995; P. Ziegler, 1975). After the Caledonian uplift during the Devonian, most of the Southern North Sea persisted as an elevated region characterized by overall erosion during the Devonian period, about 410 to 360 million years ago (North Sea

Geology, 2001). After this, the Carboniferous Coal Measures were deposited over a broad east-west trending plain between the northern Caledonian ranges and the flanking Proto-Tethys Ocean (Glennie and Provan, 1990).

4.2.4 Devonian to Permian – Variscan/Hercynian Orogeny

The Variscan Orogeny, also known as the Hercynian Orogeny, extended from the Late Devonian until the end of the Paleozoic era, with its final phases taking place during the late Carboniferous. In this period, the supercontinents Gondwanaland and Laurasia collided with each other creating a mountain range east of the Caledonian mountain ranges and creating the supercontinent Pangea at the end of the Variscan Orogeny (Shelley and Bossière, 2000; Ziegler, 1977). This phase's initiation coincides with the Caledonian orogeny's conclusion, marked by a transition to a general extensional regime (Fazlikhani et al., 2017; Ziegler, 1975). The extensional tectonic activity created conditions conducive to basin subsidence, facilitating the accumulation of sediment (Ziegler, 1977). The crustal extension started in the Carboniferous, about 360 million years ago, with the collapsing of the Caledonian orogeny, creating different grabens (Ziegler, 1977). In these grabens, up to 4000 meter of deep-water or deltaic sediments were deposited (Balsen et al., 2002).

4.2.5 Permian

During the Permian, the Variscan foldbelt was subjected to postorogenic uplift, which resulted in a period of extensional tectonics in the North Sea Basin, leading to the development of rift basins. The Permian rift basins include the Northern Permian Basin and the Southern Permian Basin, which later evolved into the Central Graben and Viking Graben, respectively. The basins were separated by the east-west trending Mid North Sea-Ringkøbing-Fyn system of highs and this was accompanied by volcanic extrusions (Glennie and Provan, 1990). Volcanoes were active at this time along the flank of the Ringkøbing-Fyn high, and locally on the Mid-North Sea high (Rasmussen, 1974). During the Permian, the Rotliegend group was deposited. In the Southern Permian basin Rotliegend dune sandstones, wadi and lake-margin sediments, are the primary gas reservoir in the southern North Sea and the adjacent Netherlands and German onshore areas (Glennie, 1972; Glennie and Provan, 1990). During the Late Permian, the southern basin sank more quickly than it accumulated sediment, causing the shallow desert lake to grow into a much larger inland sea known as the Zechstein Sea. The salinity of this sea increased to such large concentrations during marine transgression that the Zechstein Group, which comprises cyclical evaporitic successions, was deposited and can reach thickness up to 1000 meter (Brouwer, 1972; Balsen et al., 2002). Therefore, by the conclusion of the Permian period, the Southern Permian Basin possessed the fundamental elements necessary for the formation of a hydrocarbon province: Carboniferous source rock, Rotliegend reservoir, and Zechstein seal (Glennie and Provan, 1990).

4.2.6 Triassic

The Early Triassic was dominated by extensional stresses, with the creation of the North Sea rift, the subsidence of the Variscan mountains and the formation of the Tethys Ocean. This occurred as a response to the Arctic-North Atlantic rift zone (Hallam, 1971; Ziegler, 1975; Ziegler, 1977). Consequently, the formation of a new set of narrow rift and graben systems formed in the North Sea basin, with the Southern Permian Basin starting to subside (Glennie and Provan, 1990; Ziegler, 1975; Ziegler, 1977). In the Triassic, the climate changed, with a return to arid, continental climate conditions, in which rapid alternations of sand-, silt, and mudstone redbed successions were laid down (Kent, 1975; Balsen et al., 2002). In the North

Sea basin, the presence of thick Zechstein salt deposits coinciding with Triassic depocenters led to halokinetic movements during the Late Triassic period, due to the substantial thickness of Triassic sediments, that potentially remained until the Tertiary and influenced the basin on a local scale (Rathey and Hayward, 1993; Ziegler, 1977). This happened around 230 million years ago and led to the formation of salt pillows and salt diapirs in the Central North Sea area (De Jager and Visser, 2017; Balsen et al., 2002).

4.2.7 Jurassic

During the Early Jurassic period, the breakup of the supercontinent Pangea resulted in the formation of two separate landmasses known as Gondwana and Laurasia. This breakup occurred during the Kimmerian tectonic phase for most of the Mesozoic until the early-mid Cretaceous and marks the start of creating the present position of the continents today (Sun et al., 2016). The location of the North Sea basin was at the transitional zone of the separating continents, as the Atlantic Ocean started to open (De Jager and Visser, 2017). The extensional forces generated by this separation led to the stretching and thinning of the subsurface within the basin, resulting in the formation of fault lines and rift systems, providing space for sediment accumulation (Balsen et al., 2002). These sedimentary rocks comprise of alternations of marine and non-marine sediments, as throughout the Jurassic period, cycles of marine trans- and regressions were noticeable in the North Sea basin. The North Sea basin was filled with eroded sediments from adjacent landmasses transported by rivers and marine currents. The rocks that were formed are sand-, mud-, and limestones. During the Jurassic, multiple subbasins were formed including the Viking Basin, the Central Basin, the Moray Firth basin, and the Southern North Sea Basin due to the rifting processes in the region (Boldy and Brealey, 1990; Davies et al., 1996; Fisher and Miles, 1983).

4.2.8 Cretaceous

The newly formed basins that are formed on the transition between the Cretaceous and the Jurassic are accompanied by a phase of halokinesis (De Jager and Visser, 2017; De Lugt et al., 2003; Van Wijhe, 1987). In the Viking Graben, the rifts associated with the Late Kimmerian phase manifested as a prominent, blockfaulted submarine relief reaching depths of 2000 to 3000 meters. Conversely, rift tectonics in the Central Graben were less conspicuous due to the substantial diapirism of the Zechstein salts. During the Lower Cretaceous, the topography of the North Sea rift became gradually buried in a thick shale sequence, which was interrupted during the early Albian by a minor Austrian rifting phase, following the basin-wide transgression during the Albian and Aptian epochs, substantial deposits of shale were laid down. Subsequently, during the late Cretaceous period, a significant accumulation of chalk occurred (Glennie and Provan, 1990; Ziegler, 1977). By the end of the late Cretaceous, the North Sea had reached its current position and the regional stress shifted towards North America, eventually leading to the North Sea failed rift system (Rathey and Hayward, 1993).

4.2.9 Tertiary

The North Sea, as it exists today, largely took shape during the Tertiary Period, which occurred from approximately 66 million years ago to 2.6 million years ago. The opening of the Atlantic Ocean continued, as well as the collision of the Eurasian and African Plates, which resulted in the formation of the Alpine Orogeny (Ziegler, 1977). At the Paleocene, the Laramide Tectonic phase started and sediments of transgressive marine, sandy and clay sediments were deposited. During the Eocene, the last part of the Laramide Orogeny caused a stretching regime in the North Sea basin (Ziegler, 1975; Ziegler, 1977). As a result, the

North Sea basin subsided, and coastal sands and clays were deposited. The stretching regime caused volcanism during the Early Eocene and covered northwest Europe with tuff. In the Oligocene, regression occurred due to sea level rise. A vast, shallow sea covered the Netherlands and formed uniformed marine deposits. During Oligocene-Miocene, the final inversion, the Savian Tectonic Phase, caused regional uplift and a low sea level, which led to the regional erosion of Upper Oligocene sediments. Finally, the modern position of the Netherlands was accentuated during the Miocene and Pliocene (Rasmussen, 2009; Rasmussen and Dybkjær, 2020; Stouthamer et al., 2015).

5 Data & Methodology

5.1 Dataset and Samples

5.1.1 Dataset

The K06-04 well (well code: K06-D-01) is situated within the K6 block and the K06-D field, offshore of the Netherlands in the North Sea (Figure 1). The core starts at a depth of -39 m/MSL, while the rotary table stood at a height of +31 m/MSL. The spudding of the well started on August 31, 1988, and drilling operations ceased on November 23, 1988, with the primary objective being the exploration of hydrocarbons. The project was overseen by Elf Petroland B.V. and financed by various companies, including Petroland, EBN, Total, Eurafrep, Copraland, and Corexland, with Transocean DLNG Co. serving as the contractor. The well reached a final depth of 4060 meters with respect to the rotary table, encountering diverse lithologies throughout the wellbore (Table 1). The Lower Slochteren Member (Onder-Slochteren Laagpakket) was identified as gas-bearing, hosting a proven gas column of 53 meters with the reservoir base at 3824 meters. Extraction of this gas spanned from January 2003 to November 2023 (NLOG, 2024).

Stratigraphical Unit	Top (in m)	Bottom (in m)
Boven-Noordzee Groep	0.00	660.00
Midden-Noordzee Groep	660.00	720.00
Laagpakket van Asse	720.00	817.00
Mergel van Brussel Laagpakket	817.00	918.00
Laagpakket van Ieper	918.00	1304.00
Basale Dongen Tuffiet Laagpakket	1304.00	1312.50
Landen Klei Laagpakket	1312.50	1330.00
Ekofisk Formatie	1330.00	1369.50
Formatie van Ommelanden	1369.50	2511.00
Plenus Mergel Laagpakket	2511.00	2513.00
Texel Mergelsteen Laagpakket	2513.00	2627.00
Boven-Holland Mergel Laagpakket	2627.00	2667.00
Midden-Holland Kleisteen Laagpakket	2667.00	2677.50
Onder-Holland Mergel Laagpakket	2677.50	2701.50
Vlieland Kleisteen Formatie	2701.50	2783.00
Rogenstein Laagpakket	2783.00	2897.00
Hoofd-Kleisteen Laagpakket	2897.00	3051.00
Zechstein Boven-Kleisteen Formatie	3051.00	3061.00
Z2 Zout Laagpakket	3061.00	3537.00
Z2 Basale Anhydriet Laagpakket	3537.00	3542.00
Z2 Carbonaat Laagpakket	3542.00	3551.50
Z1 Anhydriet Laagpakket	3551.50	3575.50
Z1 Carbonaat Laagpakket	3575.50	3578.00
Koperschalie Laagpakket	3578.00	3579.50
Silverpit Formatie	3579.50	3820.00

Onder-Slochteren Laagpakket	3820.00	3874.00
Hospital Ground Formatie	3874.00	4060.00

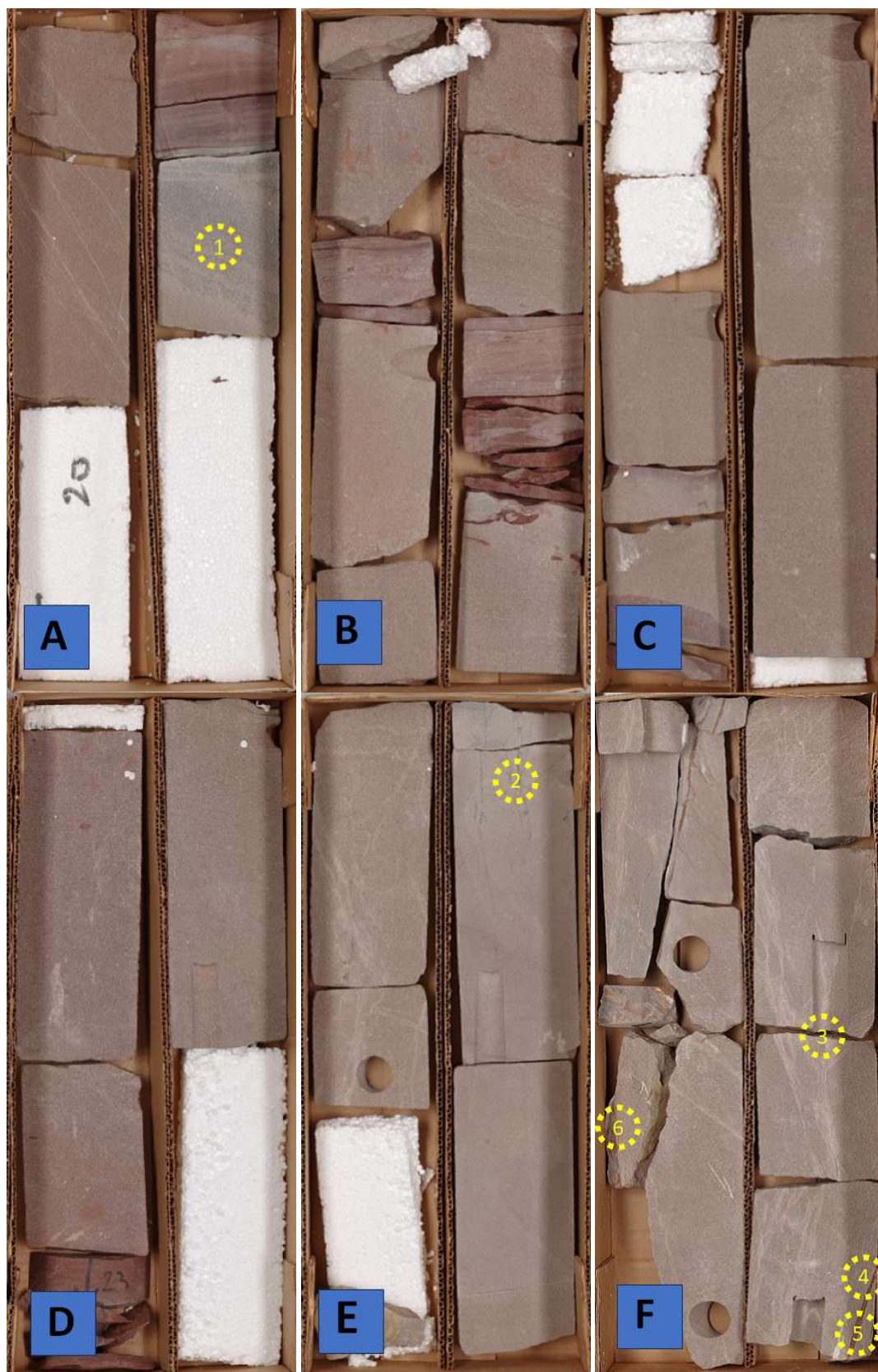
Table 1: Stratigraphical units measured along the borehole with respect to the rotary table. Table from NLOG (2024).

Three distinct cored intervals are extracted from the K06-D-01 well, with the studied interval focusing on the K06-04 core, between 3844 and 3853 meters in depth (Table 2) (Figure 2). This interval encompasses the Lower Slochteren Member, characterized by grey-beige to grey brown, poorly sorted sandstone with grains that are subangular to subrounded in shape, containing siliceous input, and cemented together by a mixture of calcite and dolomite. Additionally, it can contain interbeds of red-brown, silty to sandy, micaceous claystones. The Slochteren Sandstone Member is underlain by the Maurits formation, consisting of varicolored, silty, micaceous, and finely interbedded sandstones with siliceous cement, enclosed within red brownish claystones. At the top, the Slochteren sandstones are capped by the Silverpit claystone, characterized by red-brown, silty to very fine sandy, slightly calcareous, micaceous, and slightly anhydritic claystone. Interspersed within are whitish, red-brownish micaceous siltstones with argillo-calcareous cement, as well as very fine and silty green-grey, whitish, silty, sandy, and calcareous-dolomitic claystones.

Cores	Driller depth m/RT	Logger depth m/RT	Recovery		Stratigraphy
			m	%	
1	3831-3843	3832.7-3844.7	11.5	96	Lower Slochteren Member
2	3843-3860	3844.7-3861.7	16	94	Lower Slochteren Member
3	3900-3910	3902.5-3912.5	8	80	Maurits Formation

Table 2: Different cored intervals from the K06-04 well. The studied interval is between 3844 and 3853 m. Table retrieved from nlog.nl.

In 1998, both horizontal and vertical core plugs were taken. Porosity, permeability, and density measurements were obtained for each plug. The porosity measurements displayed considerable variation, spanning from 3.8% to 19.3%. Moreover, permeability exhibited significant variability, with values ranging from 0.01 mD to 172 mD for the horizontal plugs and from 0.01 mD to 145 mD for the vertical plugs. However, the section's density remained relatively constant, with values ranging between 2.55 g/cm³ and 2.71 g/cm³ (NLOG, 2024).



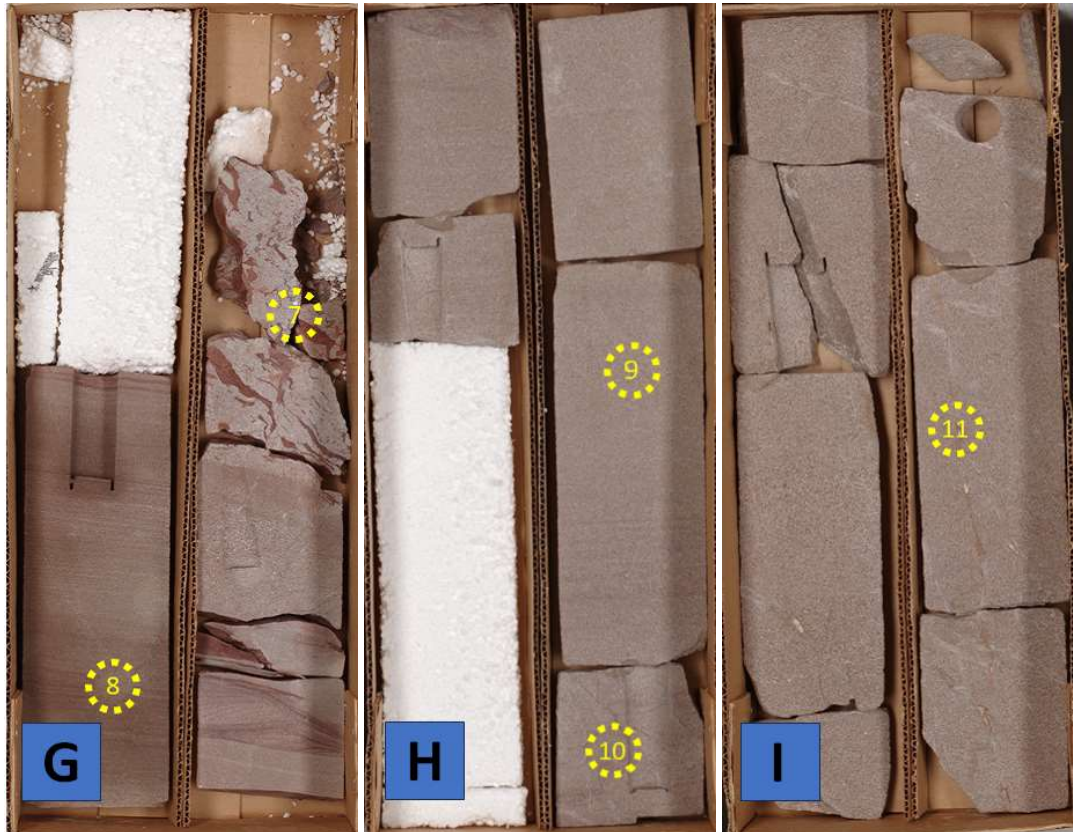


Figure 2: Core slabs of the K06-04 core that were used throughout this study with the locations of the thin sections are shown and range from 1 to 11. Images modified after Robertson et al. (2023).

5.1.2 Samples

Eleven uncovered, highly polished thin sections with blue dyed porosity were prepared from the K06-04 core by Petrographica. Petrographic analysis was conducted on these sections, taken from various locations within the K06-04 core spanning depths between 3844 and 3853 meters (Table 3). The selection of locations was based on the representativeness of the core, with a focus on identifying deformation structures and areas indicative of fluid flow (Figure 2).

Thin Section / Sample Number	Depth	Box	Optical microscope	SEM	CCL	SWIR-analysis	Description/Features
1	3844.20	2					Bitumen in specific sedimentary layers
2	3848.05	6					Bitumen filled fractures
3	3849.30	7					Deformation bands
4	3849.40	7					Top part of fault zone
5	3849.45	7					Clay fracture with main fault zone
6	3849.85	7					Clay fracture that ends on main fault zone
7	3850.15	8					Blackened fault surface
8	3850.90	8					Sedimentary structures
9	3851.20	9					Sedimentary structures
10	3851.45	9					Deformation bands
11	3852.25	10					Dolomite and clay filled fracture zone

Table 3: Thin section and sample number with a short description of the key features found. If a cell is green, the specific technique is used on the thin section/sample. The depth is an estimate. Table modified after Robertson et al. 2023.

Eleven different samples were taken for an analysis with the hyperspectral scanner (Table 3). These samples needed preferably to be taken at the exact location of the thin sections. As the thin sections locations within the core were missing, the scanned sample locations had to be determined at different locations. Therefore, nearby locations were selected either based on interpreted similar mineralogical composition or from areas opposite the saw cut. Consequently, these selected locations could deviate a maximum of a few centimeters horizontally or vertically from the thin section's location. Second, the height of the sample needed to be small enough to fit under the hyperspectral scanner. Therefore, samples needed to be cut or sanded before they were scanned. The samples were no larger than 20 mm in height. Another concern was to remove any surface contaminants and the sample needed to be free from dust and dry. For cleaning, pressurized air is used. The samples used did not need to be completely flat, and therefore sanded or polished; some relief in the sample was acceptable.

A short overview of the thin sections and samples can be found in Table 3, along with the methods used for each thin section/ sample. Images of the samples can be found in the 'Hyperspectral scan locations' PowerPoint.

5.2 Methodology

5.2.1 Petrographic analysis

Three different microscopes are used for the petrographic analysis: the optical light microscope, the scanning electron microscope, and the cathodoluminescence microscope.

5.2.1.1 Optical Light Microscope and Point Counting

Thin sections as seen under an optical light microscope were digitized into Carl Zeiss Image (CZI) files using the Zeiss AxioScan, located within the Earth Simulation Laboratory. This system captures high-resolution images of optical light microscope slides under plane-polarized and cross-polarized light at six orientations, facilitating detailed mineralogical characterization. The point-counting process was done in JMicroVision v1.3.4 to quantify the analyzed features. JMicrovision was designed especially for the analysis of high-definition images of rock thin sections and has the function of describing, measuring, quantifying, and classifying components of all kinds of images. The purpose of quantitative petrography is to quantitatively understand the information in the core rocks and the thin section samples. Quantifying the rock components in host rock and deformation features in this way serves as comparison for the quantitative results obtained by hyperspectral scanning of the core surface. For each of the thin sections, a point count was done on 250 points to estimate the relative abundance of each mineral. For this number was chosen as it is a balance between statistical significance and practical feasibility (Appendix; Figure 5). As mentioned, the point counting of the thin sections focused on various aspects, including deformation structures and zones of fluid flow. The relative abundance of the minerals in a thin section might therefore not be the right representation of the host rock mineralogy. Overall, assigning a mineral to a specific mineralogical class was based on the plane polarized and cross polarized light microscopic image of the thin section. Point counts were done on the whole thin section, so no regions of interest were chosen.

The following categories were used throughout the point counting process:

Dolomite (vein, cement)

Clay (vein, cement)
Kaolinite (vein, cement)
Illite (vein, cement)
Quartz
Feldspar
Lithic grain
Bitumen
Heavy minerals (zircon, barite, rutile)
Porosity (primary, fracture, vuggy)

In the analysis, specific attention was given to distinguishing between vein and cement minerals to visualize potential variations in quantity. This distinction was based upon the textural and mineralogical differences between the two. However, it sometimes appeared to be difficult to precisely distinguish where the boundaries of the cement and the veins are. In those cases, the most obvious choice was made.

Not all minerals could be identified using the light microscope. For instance, differentiation between dolomite, ferroan dolomite, siderite or ankerite was challenging. In such cases, they were categorized as 'dolomite'. Similarly, distinguishing between distinct types of clays, such as illite or kaolinite, proved sometimes difficult in the matrix, leading to their classification as 'clay' if no distinction could be made. The porosity in the samples were classified as primary, fracture and vuggy. The primary porosity is that developed during the concluding sedimentation phase or was present in the sedimentary particles during deposition. The fracture porosity is formed during fracturing and occurs along breaks in the sediment, while the vuggy porosity is a porosity type formed during dissolution that has relatively large, somewhat equant pores that can be seen with the unaided eye. The non-primary porosity types are all secondary porosity (Choquette and Pray, 1970; Mazullo, 2004).

5.2.1.2 Scanning Electron Microscope

The scanning electron microscope is used to better constrain crystal morphology and to identify mineral components that are indistinguishable using optical light microscopy. This includes the distinction between quartz and feldspar and the identification of the different types of clays and dolomites. Moreover, the textures and fracture composition encountered in the thin sections were studied.

For this analysis, two different thin sections, thin section 3 and 6, were chosen for an analysis with the scanning electron microscope (SEM). Thin section 3 appeared to have a relatively high feldspar content, while fractures were clearly visible within thin section 6. For the analysis, the SEM in the Electron Microscopy Centre at Utrecht University was used. This SEM is incorporated with an energy dispersive system (EDS) to better constrain the crystal morphology and identify mineral components that cannot be distinguished solely with the optical light microscope. Both samples were coated with a carbon coating and two copper strips, positioned adjacent to both sides of the samples, were placed to mitigate the buildup of electric charge on the sample's surface. The selected accelerating voltage for the measurements was 15 kV. The SEM that was used was a Zeiss EVO 15 environmental SEM, while the secondary electron images were made with a Bruker XFlash 6160 (Figure 3). During SEM analysis, backscattered secondary electron (BSE) images provide insights into the distribution and composition of minerals and are used to identify and better understand the spatial distribution of minerals. Elements with higher atomic numbers tend to scatter electrons more effectively, resulting in brighter areas in the BSE image. Conversely, elements with lower atomic numbers produce darker areas.



Figure 3: Scanning Electron Microscope in the UU Electron Microscopy facility that was used to study thin sections 3 and 6.

5.2.1.3 Cold Cathodoluminescence

Cold cathodoluminescence involves bombarding the sample with high energy electrons. This results in the emission of characteristic visible luminescence from specific substances (Boggs and Krinsley, 2006). Thin sections 1 and 11 were taken for the analysis with an optical cold cathodoluminescence microscope, as these thin sections were the lowest and highest positions within the core.

Emphasis was put upon the dolomite cement, different clay types, the rimming of the quartz grains, the feldspar content, and the type of minerals present around the fracture zones. The cold cathodoluminescence microscope that was used is the Technosyn 8200 Mk II Cold Cathode Luminescence, while the photos were taken with a Nikon D810 digital camera. After the thin section chamber was vacuumed, the analysis could begin with the cathodoluminescence microscope. The beam current of the electron gun was about 300 microamperes, while the acceleration voltage used was greater than 10 kV, but never exceeded 20 kV.

After the results of the SEM and the CCL were analyzed, it became clear that feldspar content was overestimated during the point counting analysis. Grains identified as feldspar turned out to be often lithic grains or polycrystalline quartz. Based on that information, the point counting results were revised and recounted, if necessary.

5.2.2 Hyperspectral Imaging

For the identification of the different minerals in the samples, the hyperspectral imaging scanner is used to obtain the characteristic spectral response of the minerals to infrared

light (Savitri et al., 2021). The infrared spectrum can be subdivided into different groups and includes visible to near infrared (VNIR), short-wave infrared (SWIR), and long-wave infrared (LWIR) (Savitri et al., 2021; Kraal and Ayling, 2019; Nikonow et al., 2019). The focus for this report is on the SWIR, with wavelengths between 1000–2500 nm. Different minerals produce different absorption features in the SWIR when they interact with the electromagnetic radiation, which is known as their spectral signature (Kraal and Ayling, 2019; Laukamp et al., 2021). The identification of this SWIR hyperspectral imaging is limited to minerals that contain OH or H-OH bonds in the mineral structure and is therefore the best for the identification of phyllosilicates (including illite and kaolinite), amphiboles and carbonates (Nikonow et al., 2019; Kraal and Ayling, 2019). Absorption features of these OH and H-OH bonds are different for specific groups. The absorption features of AlOH are between 2186 and 2225 nm and have a weaker secondary feature between 2344 and 2440 nm. The Fe-OH absorption feature is found between the wavelengths of 2235 and 2265 nm, while the Mg-OH feature can be found at higher wavelengths between 2320 and 2350. The CO₃ feature, diagnostic for carbonates can be found between 2300 and 2350 nm and is significantly weaker than the phyllosilicates (Huang et al., 2018). Non-hydroxylated silicate minerals, including garnets, feldspars, and quartz cannot be detected as they do not have diagnostic absorption features in the shortwave infrared range (Hecker et al., 2019).

5.2.2.1 Apparatus

The apparatus that was used for the acquisition of the short wavelength infrared (SWIR) images consists of the Specim spectral camera equipped with the SWIR Enhanced Series OLES Macro-Lens (Figure 4). This camera setup is in the Geo-Science Laboratory at the University of Twente, Faculty ITC, Enschede, the Netherlands and can collect a continuous hyperspectral data set from the samples that consists out of 288 bands in the wavelength range between 926.80 to 2542.70 nm. Table 2 provides detailed technical specifications of the camera used in this study. Subsequently, the hyperspectral images are processed and analyzed using two software programs: Hyperspectral Python (Bakker, 2012) and ENVI (NV5 Geospatial Solutions, Inc, 2024).

Lab stage setup	
Spectral range (nm)	926.80-2542.70
Pixel size (μm)	26
Image swath (mm)	10
Number of bands	288
Lens focal length (mm)	73.3
Spectral sampling (nm)	5.6
Spectral resolution FWH (nm)	12
Frame rate (frame/s)	9.50
Scan speed samples (mm/s)	10
Scan speed white reference (mm/s)	15
Exposure time (ms)	8.00

Table 2: Technical Specifications of the hyperspectral scanner used during this study.



Figure 4: Hyperspectral scanner at the ITC Twente that was used to study 11 different core samples.

5.2.2.2 Sample Preparation and Scanning Procedure

The samples were placed in a small box with sand with a light absorbing cloth underneath it to reduce the background noise. If the bottom of the sample was irregular, the sand and some external materials were used to make the top of the sample horizontally aligned. The sample was placed in the center of the box, with the box placed 3 centimeters from the edge of the rotating platform. After this was done, the height of the platform was in- or decreased to make sure that about half of the thickness of the laser was in line with the top part of the sample. Then, the sample was placed under the SPECIM SWIR camera, and the data acquisition could start.

The width of the image swath of the SWIR camera is 10 mm. As all the samples exceeded this width, multiple scans were needed to scan the whole sample. The platform was moved from right to the left each time with 8 to 9 millimeters to create some overlap between the scans. This was done until the sample was fully scanned. The sample was checked in the image viewer of the HypPy software to make sure that a) the sample was in focus, this makes no difference for identification of the minerals itself and b) parts of the samples showed overlap to make sure that the full sample was indeed scanned.

In case the platform could not move any further to the left, the sample was manually moved so the scanning could continue. As a result, a sample could be scanned in different segments. This is the case for sample 11. Initially, the middle section, where the fracture is visible, was scanned. Subsequently, the right-hand side and then the left-hand side of the sample were scanned.

5.2.2.3 Pre-Processing

5.2.2.3.1 *Conversion*

The first step was to convert the raw digital number values (DN) into the reflectance image using the dark & white reference tool in the HypPy3 software.

5.2.2.3.2 *Mosaicking*

Between the different scanned strips, overlap is visible. To remove this overlap, the ENVI software is used. With this software, pixel perfect mosaicking can be achieved. As mentioned, sample 11 was manually moved, in this case, the left, middle and right part of the sample were scanned separately. Therefore, pixel perfect mosaicking could not completely be achieved for this sample. Also, during the movement of the platform, the box of the sample or the sample itself might have moved slightly. Therefore, pixel bands can sometimes still show some minor overlap. Nevertheless, the best possible mosaic was tried to achieve. During the mosaicking, no color balancing or feathering is used.

5.2.2.3.3 *Subset/Convert*

The subset/convert tool of HypPy is used for making spatial and spectral subsets of the obtained hyperspectral images. After the overlap between the strips was removed, a final image of the scanned sample was created. When large black bands were visible on the top and the sides of the sample, were these, if possible, removed with the spatial subset. As a result, minor parts of the sample's edges were removed. This was done to make an easier analysis of the sample and to decrease the file size.

During the spectral subset, specific bands at the beginning and end of the spectral range were excluded. This was necessary because each image contained unwanted bands that needed to be eliminated to ensure accurate analysis. The bands within the range of 1001.00 to 2520.25 were chosen for further examination and processing. This selection was made to focus on the spectral data most relevant to the project's objectives. The first 13 bands (926.79 to 995.27 nanometers) and the last 4 bands (2525.86 to 2542.69 nanometers) were excluded from the spectral data due to noise or distortions, making them unsuitable for analysis. This was done to make sure that only meaningful spectral information is analyzed and enhance the quality of the outcomes.

5.2.2.4 Processing

As part of the data processing, some summary products have been derived to facilitate detailed image analysis. These include ferrous drop, mixture ratio, illite vs kaolinite, and illite crystallinity.

The ferrous drop is the ratio of reflectance values at the 1600 nm and the 1310 nm band, serving as an indicator of iron-bearing mineral features. High values correspond to a steep slope, indicating a higher concentration of ferrous iron within the mineral's crystal structure. Consequently, increased ferrous drop values are characteristic of minerals such as ferroan dolomites and siderite.

Because of the small grain sizes present in the core, the pixels that have been scanned might include different spectral profiles of carbonates as phyllosilicates. The mixture ratio determines the difference between the depth of the carbonates and the phyllosilicates. It

does this by taking the deepest feature between 2140-2280 nm and subtracts this from the deepest feature between 2200-2390 nm.

The illite vs kaolinite ratio is used to distinguish between kaolinite and illite. Kaolinite has a doublet absorption feature, a spectral signature characterized by two closely spaced absorption bands in a spectrum, near 2200 nm, which is absent in other phyllosilicates. For the illite vs kaolinite ratio, the peak of the doublet feature is divided by the previous trough. Because of this feature, kaolinite has relatively low values for the illite vs kaolinite ratio, while illite on the other hand has relative high values.

The illite crystallinity is used to distinguish between crystallinity values in the samples as illite, illite-smectite, and smectite have similar positioned absorption features. The ratio is calculated between the depth of the water absorption features at around 1900 nm divided by the water feature at around 2200 nm. As the water features become less intense with a higher degree of crystallinity, the ratio shifts. Low crystallinity values indicate a more smectite rich composition, with high values being an indication of muscovite (Brouwer, 2022).

5.2.2.4.1 *Wavelength Of Minimum*

This tool determines the wavelength of the deepest feature below the smallest convex shape that encloses all the spectral signatures of materials present in a hyperspectral imaging dataset, the spectral hull. If a range is defined using start and end, then the minimum is determined within this wavelength range.

For the wavelength mapping, four different wavelength of minimum files were made, each having their own range between: 1300-1650 nm, 1650-1800 nm, 1800-2100 nm, and 2100-2400 nm. Chosen for these four ranges is because each of them displays diagnostic mineralogical information about the active spectral absorption features within them. For these files, the convex hull used is the divide option and the three deepest features were determined. The program generates the wavelength of the first local minimum, the depth of the first local minimum, the wavelength of the second local minimum, the depth of the second minimum, the wavelength of the third local minimum, and the depth of the third minimum (Appendix; Figure 6).

For the mixture ratio, an input for the decision trees, two different wavelength of minimum files were made. These files had ranges between 2140-2280 nm and between 2200-2390 nm. These two ranges were chosen as they calculate the first ALOH-feature and the second ALOH or carbonate-feature. For these files, the convex hull used is the divide option and only the deepest feature is determined.

The wavelength positions of the deepest features are determined by a second-order polynomial that is fitted to three consecutive bands, of which the center has the lowest reflectance. As a result, absorption features of similar depth, such as doublet features, might not be determined.

5.2.2.4.2 *Wavelength Mapping*

This tool takes the output of the previous wavelength of minimum tool and produces a color map by using a color table on the interpolated wavelength of minimum and the Hue, Saturation, and Value color model (HSV) merges it with the interpolated depth of the feature. The two bands that resulted from the first step were combined, where the wavelength position determined the hue, and the depth controlled the intensity of the color image. To color all

the pixels, the lowest value of the automatic depth stretch was used as largest value for the stretch for depth.

5.2.2.4.3 *Band Ratio*

The band ratio tool calculates the ratio of two specified bands, resulting in a one-band float image representing their ratio. This is done to characterize specific mineral properties present in the different samples. The tool determines the ratio of two peaks at specific wavelengths. Two distinct band ratios were established: the ferrous drop, which is the ratio of the band at 1600 nm divided by the band at 1310 nm and the illite over kaolinite, which is identified as the band at 2195 nm divided by the band at 2178 nm. Both spectra have not seen a convex hull correction.

5.2.2.4.4 *Band Math*

In the assessment of illite crystallinity and Mixture ratio, the band math tool within the HypPy software platform is used. Specifically, for the determination of illite crystallinity, the deepest spectral feature within the wavelength range of 1800 to 2100 nm is quantified and divided by the deepest feature within the wavelength range of 2100 to 2400 nm. This ratio provides a measure of illite crystallinity, indicative of the relative abundance of illite minerals within the sample.

Conversely, for assessing the mixture ratio, spectral analysis is conducted within the wavelength intervals of 2140 to 2280 nm and 2200 to 2390 nm. The Band Math function is then utilized to calculate the difference between the deepest absorption features within these intervals. Specifically, the depth of the deepest feature within the 2200 to 2390 nm range is subtracted from that within the 2140 to 2280 nm range. This difference serves as an indicator of the mixture ratio, reflecting compositional variations within the analyzed sample.

5.2.2.4.5 *Decision Trees*

The different decision trees made by Brouwer (2022) were used to automatically assign a pixel to a specific mineral or mineral composition. These include: the first feature tree, the carbonate tree, the molecular bond tree, and the multiple aspect tree. A concise summary of these trees is given below:

The first feature tree determined the deepest feature within the 2100 to 2400 nanometer wavelength domain.

The carbonate decision tree identifies the pixels with the strongest or second strongest absorption feature between the wavelength range between 2310 and 2350 nanometer, indicative for carbonates. The carbonate decision tree uses the mixture ratio and the iron drop for the elimination of phyllosilicate pixels and further characterization of the carbonate minerals within the sample.

The molecular bond decision tree uses as primary input the position of the deepest absorption features between 2100 and 2400 nanometers. Secondary inputs such as mixture ratio, iron drop and illite vs kaolinite are used to further distinguish between the different pixels.

The multiple aspect decision tree determines three specific groups: carbonates, phyllosilicates and a mixture of the two. It does this based on the deepest and second deepest absorption feature between 2100 and 2400 nanometers. The carbonates, phyllosilicates and

the mixture of the two is further specified by the iron drop, illite crystallinity, illite over kaolinite, and the mixture ratio.

The outputs of the ferrous drop, illite crystallinity, and the illite vs kaolinite are colored with a decision tree. For the illite crystallinity and the illite vs kaolinite, carbonates that have been determined based on wavelengths greater than 2300 nanometer, are excluded. A step-by-step progression in value with different color values has been applied in every decision tree.

6 Results

For each of the different techniques, the results from the K06-04 core are summarized.

6.1 Petrography

For the petrography, the combination of the optical light microscope and point counting, CCL, and SEM was used.

6.1.1 Optical Light Microscope and Point Counting

For each of the eleven thin sections a point count was done. The percentages are listed in the Appendix; Table 1, while a graphical representation of these percentages can be seen in Appendix; Figure 1.

A distinction was made between the matrix (cement) and the deformation structures (vein). Based on optical light microscopy, at least three different fracture/fault zones were seen (Figure 5). These were filled with carbonates, clays, and bitumen.

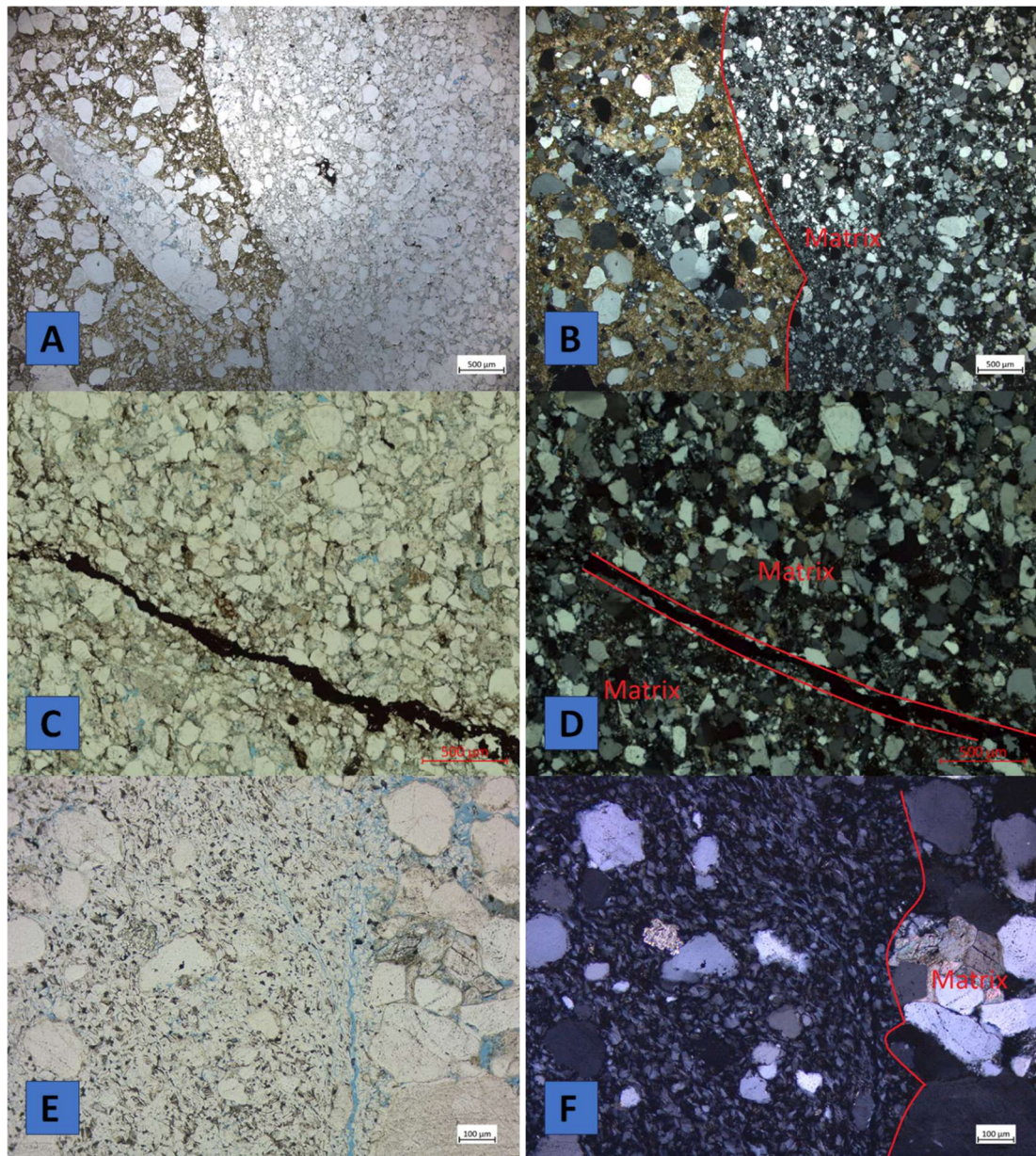


Figure 5: The three deformation structures that have been found in the thin sections. A, C, and E are under plain polarized light, while B, D, and F are under cross polarized light. The red lines separate the matrix from the veins. The images annotated with A, B, E and F are credited to Eva de Boever.

The detrital mineral assemblage identified through thin section analysis comprises primarily quartz, zircons, muscovites, and lithic fragments. Quartz is the predominant mineral phase across all eleven thin sections, with quartz content ranging from 56.4% to 72.4% (Appendix; Figure 1). These quartz grains exhibit varying sizes and morphologies, ranging from very angular to subrounded-rounded shapes. There is observable variability in quartz grain size among the thin sections, with a trend suggesting smaller grain sizes proximal to fault zones (Figure 5A; Figure 6A). Some quartz grains exhibit evidence of fracturing and fragmentation, in which their color becomes sometimes deep brown under plain polarized light (Figure 6B). Infilling with secondary materials can also be found under the optical light microscope, however, these minerals could not be determined. Lithic grains, fragments of sedimentary,

igneous, or metamorphic rocks, are identified within the thin sections, although in lesser abundance compared to quartz. Additionally, muscovites (Figure 6C), although not counted, and zircons (Figure 6D), exclusively identified with the optical light microscope, were observed, albeit in quantities not exceeding 1% (Appendix; Table 1).

Authigenic minerals observed in the thin sections exhibit distinct morphological features and distribution patterns. Authigenic quartz is frequently observed as syntaxial overgrowths along the edges of detrital quartz grains, leading to an angular shape of the grains (Figure 6E). These syntaxial overgrowths are consistently present across all thin sections and typically exhibit a maximum thickness of approximately 100 micrometers. Dolomite and clay minerals, particularly kaolinite, are the most abundant authigenic mineral phase in the thin sections (Figure 6A, F). Within the matrix of the samples and fracture zones, the rhombohedral dolomites can exceed sizes greater than 500 micrometers. Dolomite grains within fracture zones appear crushed, as evidenced in thin sections 4, 5, 6, and 11 (Figure 6A Figure 5A, B). However, differentiation between several types of dolomites (e.g., iron-rich dolomite, ankerite, and siderite) based solely on thin section analysis proves challenging. The abundance of dolomite, as determined through point counting analysis, exhibits variability ranging from 2.4% to 24.8% (Appendix; Figure 1). Clay minerals are also prevalent in the thin sections, occurring both within the matrix and as fracture fill material. Kaolinite predominates as the filling material within specific fractures (Figure 6A), while the type of clay can sometimes not be distinguished on thin section analysis alone. Bitumen, present in all thin sections, exhibits variable concentrations, with the higher concentrations observed in the fault surface (Appendix; Table 1) compared to lower concentrations in the fracture zones that are filled with dolomite and clay (thin sections 4, 5, 6, and 11). In sedimentary structures (thin sections 1, 2, and 10), bitumen concentrations are low within specific layers of the sandstones, whereas smaller fractures within these structures are often filled with bitumen (Figure 6D, Figure 5C, D).

The three types of porosity found with the point counting are primary, fracture and vuggy porosity. Noticeable is the large variability in primary porosity values between different thin sections. A clear decrease in porosity towards the fault zone can be seen in thin sections (Figure 5a). In thin section 7, the thin section of the fault surface, no porosity was determined. Also, in specific parts of thin sections, the parts where fracture or fault zones can be seen, no porosity can be determined. On top of that, the size of the primary pores changes per thin section, with the thin sections with the most primary porosity also having the largest pores and grains (Appendix; Figure 1). The largest amount of fracture porosity was found in thin section 5, especially in the clayish fractures. For the bitumen fractures, no porosity was observed, while for the dolomite filled fractures, porosity is observed between the quartz grains, while the carbonates show little to no porosity. Vuggy porosity was only counted in thin section 8. In some other thin sections, for example thin section 4 and 6, vuggy porosity was also observed, but was not counted during the point-counting analysis.

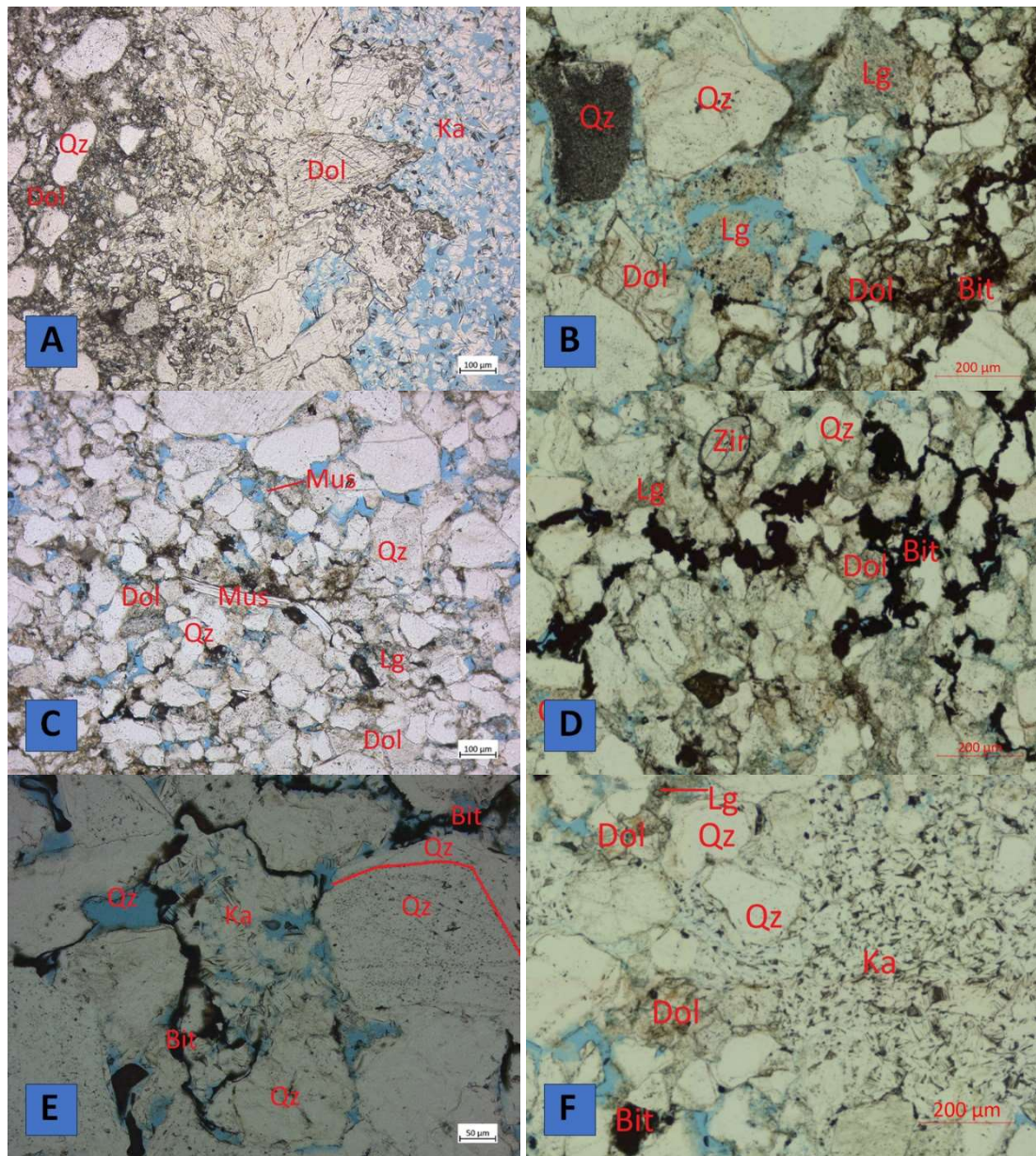


Figure 6: A) Fracture as present in thin section 11, that has been filled with dolomite and clay, surrounded by grinded quartz. B) Fracture that is filled with bitumen surrounded by a minor band of dolomite. C) Detrital muscovite, quartz and lithic grains in the matrix, with some authigenic dolomite. D) Fracture that is filled with bitumen. Quartz, lithic grains and dolomite are present in the surrounding matrix. E) Bitumen surrounding kaolinite with a quartz grain that shows clear overgrowth (authigenic quartz overgrowth separated from the detrital quartz by the red line). F) Fracture filled with kaolinite. The images annotated with A, C, and E are credited to Eva de Boever.

6.1.2 Scanning Electron Microscope

The main target of the scanning electron microscope (SEM) analysis was to find out if feldspar was present in thin sections 3 and 6. Further, the scanning electron microscope was used to get a better look in the fracture zones of thin section 6.

Detrital quartz is found not to be contaminated but occasionally, fractures or breakages may harbor other elements (Figure 7A), while no mineral composition consistent with feldspar was found. The SEM identified distinct types of dolomites in the matrix. The inner part of the dolomite is a non-ferroan dolomite (Figure 7B, C), with an increase of iron content towards the edge. Dolomite has contaminations of manganese, magnesium and sometimes calcium and aluminum in it, with magnesium concentrations sometimes higher than iron concentrations. The observed fault zone is also filled with dolomite (Figure 6D, E, F). This ferroan dolomite contains significantly more iron when compared to the dolomite in the matrix with a composition varying between 15% to 20%.

The authigenic quartz rims, that have small trace amounts of calcium and magnesium, can enclose authigenic kaolinite (Figure 7C). The kaolinite that was identified sometimes contained solely Al, Si and O, while other kaolinite had some contaminations of other elements in it, which includes K and Na. This kaolinite was identified in pores as fine crystalline (Figure 7A). Further, kaolinite was found in fractured rutile grains. Also in this kaolinite, small contaminations could be found, which include chromium, magnesium, potassium, and iron.

With the SEM, minor quantities of other minerals have been found, including contaminated muscovite. Further, barite is present as a rare authigenic phase and was only identified with the SEM (Figure 6B, D, E). The grains are no larger than about 50 micrometers and were found in the matrix and near the fault zone. The grains show slight contamination of magnesium, silicon, and calcium. Rutile is a rare authigenic phase, distinguishable exclusively through the examination of thin section 3. Certain rutile specimens display minor silicon contamination or degradation, accompanied by the presence of inclusions comprising of other minerals, such as quartz. The rutile minerals identified measure a maximum size of about 200 micrometers. Chlorite was found in sample 3 and could only be found with the SEM and contained traces of chromium.

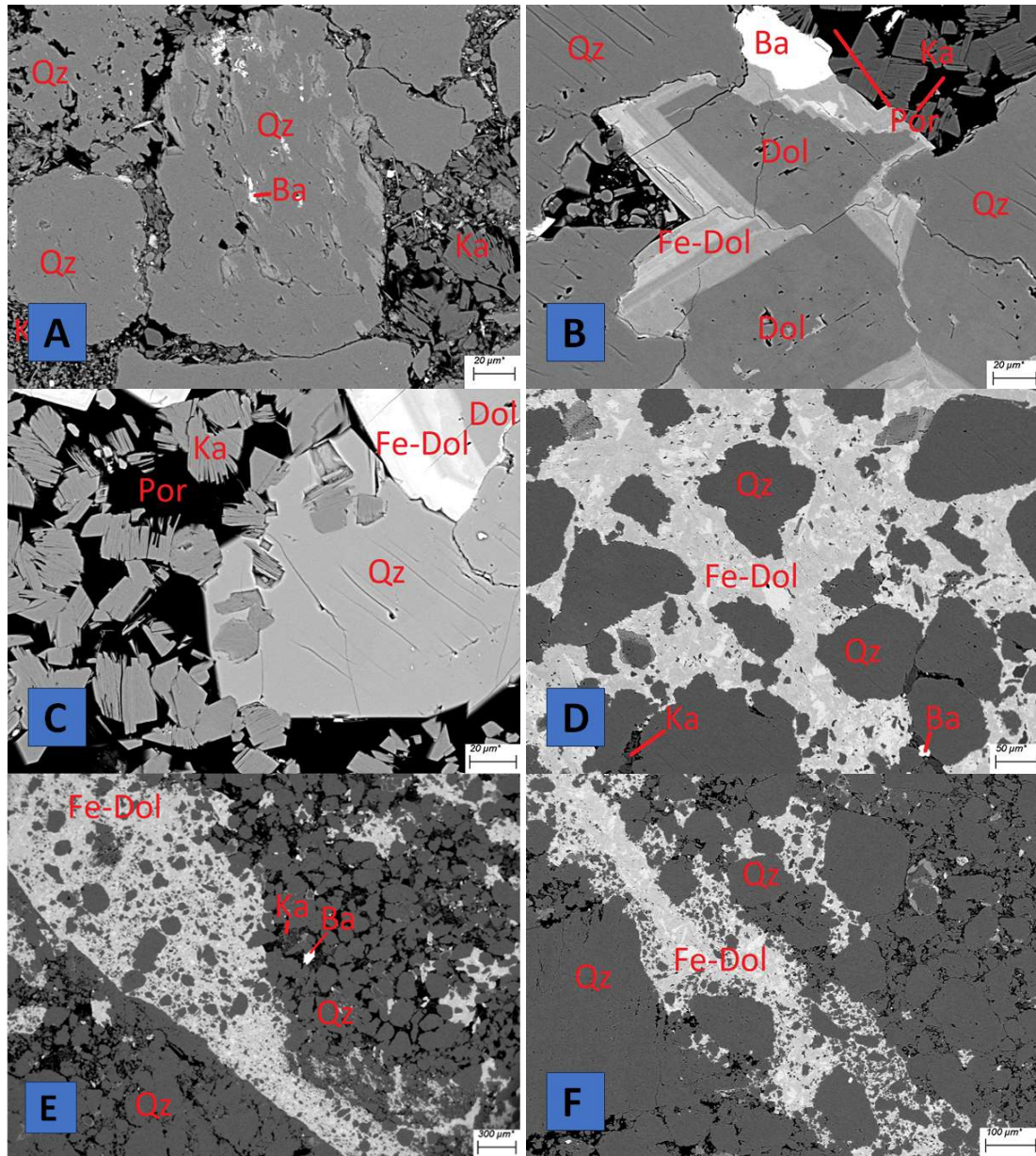


Figure 7: SEM images of thin sections 3 and 6. A) Unfractured quartz grains and fractured quartz grains of which one is partially filled with barite. B) Non-ferroan dolomite is the nucleation site for the ferroan dolomites around it. Barite, kaolinite and quartz are part of the matrix. C): Authigenic quartz rim that encloses kaolinite, along with a non-ferroan dolomite in the top corner with ferroan dolomite edges. D) Zoomed in part of the fault zone with angular quartz grains. The fault zone is filled with different types of ferroan dolomite. Note that there is still some porosity between the quartz grains. E) Fault zone as in thin section 6. Clear boundary on the bottom of the fracture. Quartz grains size reduction towards fracture zone. F): Fault zone without a clear boundary. Quartz grains are broken up towards fault zone and porosity is collapsed.

6.1.3 Cathodoluminescence

Just as the SEM, the main objective of utilizing the cathodoluminescence microscope was to differentiate between quartz and feldspar. Specific sections of thin sections 1 and 11 that

were expected to contain feldspar based on optical microscopy, were targeted for cathodoluminescence analysis (Figure 8). However, during examination using cathodoluminescence, no discernible presence of feldspar was observed within the scanned sections.

The fluorescent minerals exhibiting intense brightness are identified as dolomite. However, significant variability is observed among the dolomite specimens present. Dolomite manifests a spectrum of colors under examination, ranging from fluorescent yellow to red and eventually transitioning to black related to their iron content. When using cathodoluminescence microscopy, discernible distinctions in the luminescent properties of the dolomite specimens are observed. Notably, dolomite sourced from the fracture zone, as observed in thin section 11, appears black under CL analysis (Figure 8B). These dolomites exhibit distinctive characteristics, appearing notably fine-grained and devoid of cleavage. Some of these dolomite specimens display a bright yellow staining and occasionally feature larger grains displaying a more fluorescent reddish hue. The dolomite sourced from the matrix, however, displays a gradient of coloration, transitioning from a bright yellowish to orange hue towards a darker, mostly reddish, but sometimes blackish appearance as moved towards the outer edges.

The predominant constituent within the thin sections comprises of quartz grains. These quartz grains exhibit a range of color variations, spanning from Bordeaux red to shades of blueish red and purple (Figure 8A, B). Some of the quartz grains display visible fractures, which can be seen as they show a subtle color difference compared to the overall hue of the mineral. Within these fractures, the presence of yellowish particles is occasionally discernible. Specifically, quartz grains exhibiting pronounced breakdown often harbor larger quantities of these yellowish flakes. Moreover, the phenomenon of quartz rimming is evident. Under optical microscopy, quartz rims are notably distinguishable, presenting as discernible features surrounding the quartz grains. However, it is observed that the cathodoluminescence emissions from authigenic quartz rims are significantly less intense compared to detrital quartz grains, with instances where no emission intensity is observed at all.

In cathodoluminescence, the clays present a dark blue hue with minimal intensity variations. Within the clay matrix and sometimes the fracture zone, distinct kaolinite flakes are identifiable. Furthermore, the porosity of the sample exhibits a distinctive yellow-greenish hue. However, other minerals, including heavy minerals such as zircons, were not detected under the cathodoluminescence microscope. Similarly, bitumen, which was readily visible under optical light microscopy, eludes detection under cathodoluminescence analysis.

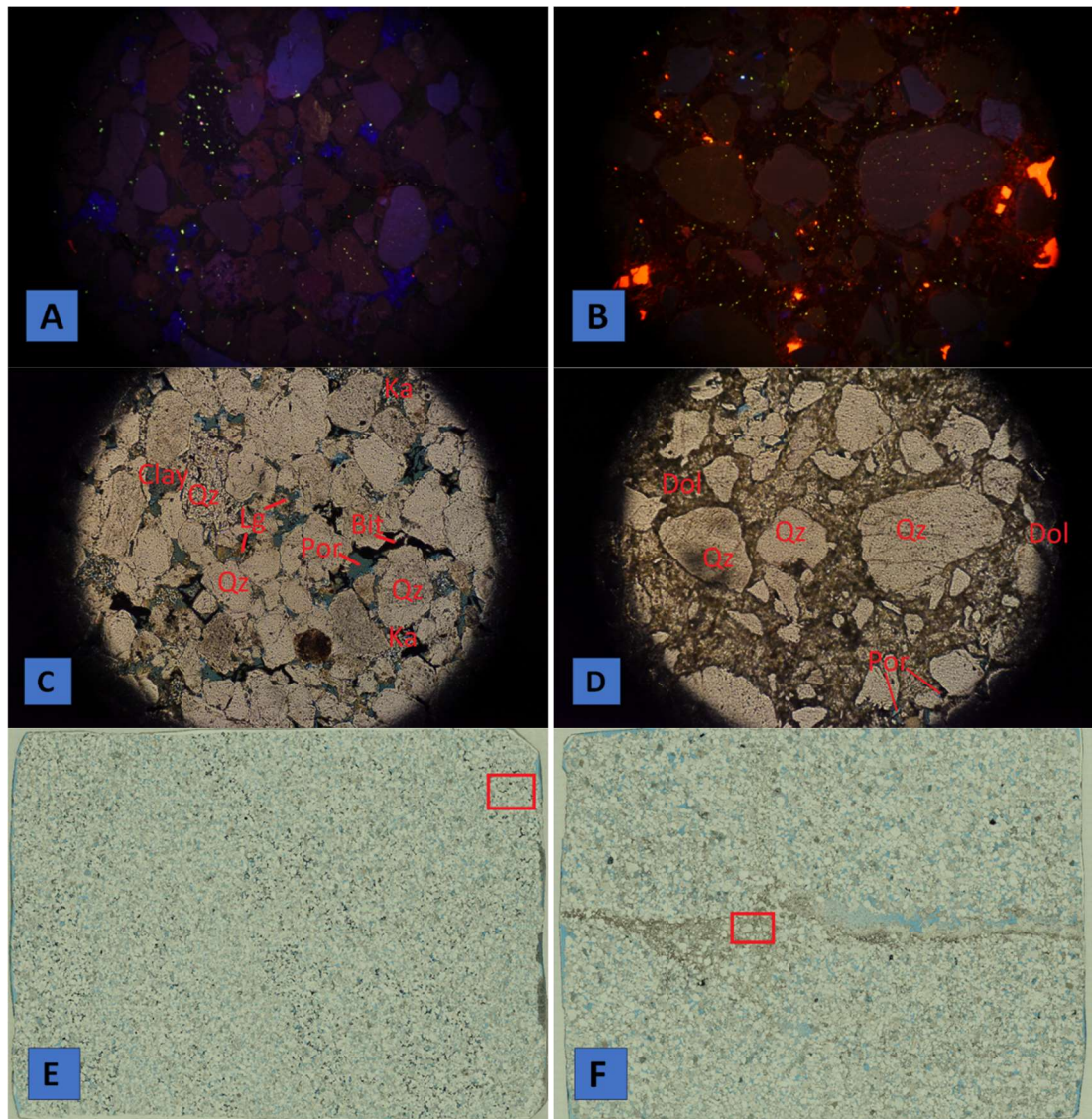
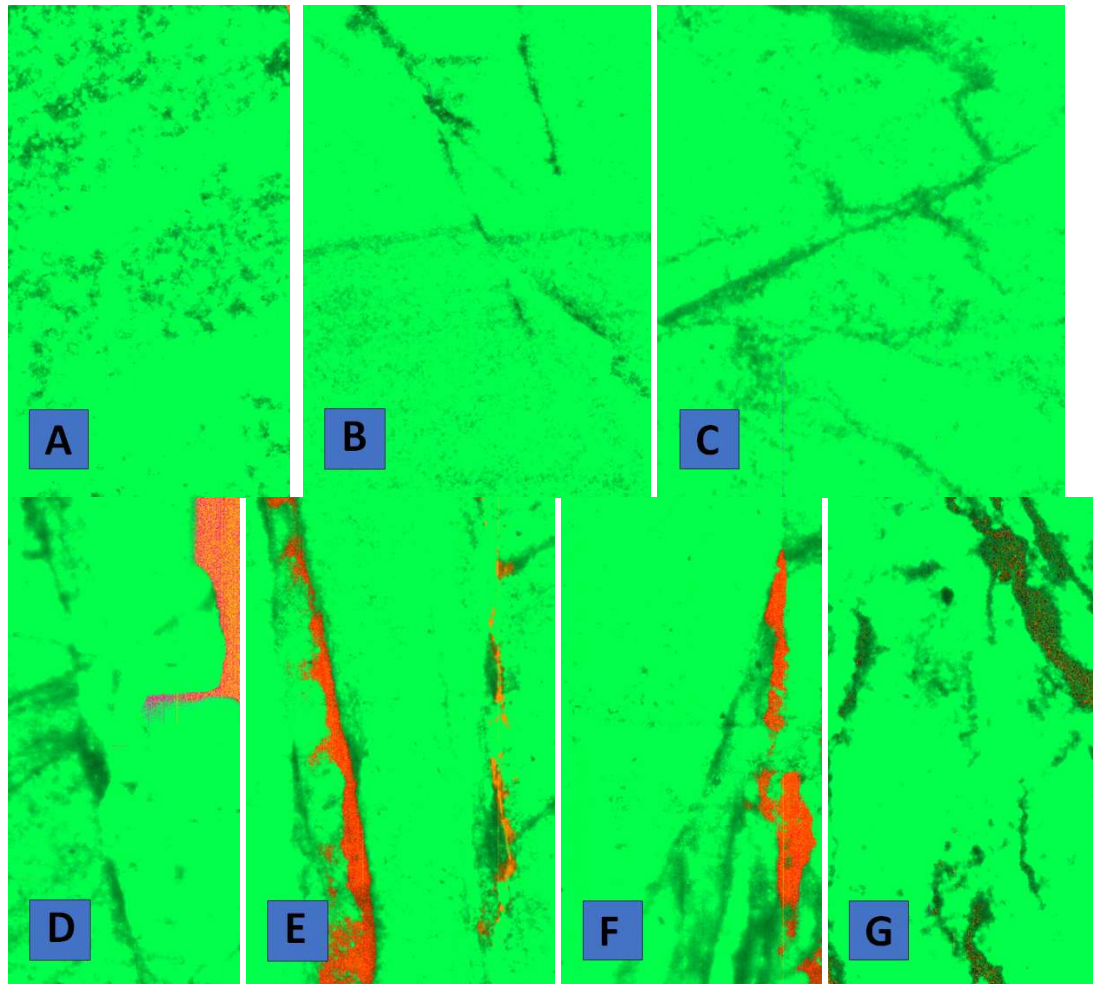


Figure 8: Cathodoluminescence microscope of the thin sections 1 and 11. A) Thin section 1 as can be seen with the CCL. Quartz grains are pinkish and vary in size, while the clays are blue. B) Thin section 11 as can be seen with the CCL. Dolomites vary in luminescence from yellow to black for the ferroan dolomites in the fault zone. C/D) Thin section 1 and 11 as can be seen with the optical light microscope. Both images are taken at the exact same location as A/B. E) Location of A/C on thin section 1. F) Location of B/D on thin section 11.

6.2 Hyperspectral analysis

Wavelength maps were made for the intervals 1300-1650, 1650-1800, 1800-2100, and 2100-2400 nm. The results for the wavelength maps for the interval 2100-2400 nm are shown in Figure 9. The main absorption features are almost all around 2200 nm for the matrix. However, the intensity of these absorption features differs. Based on wavelength mapping images, the minerals in the matrix of the samples are very similar and can be identified as clay, with sometimes a carbonate feature. The absorption features in the fault zones, however, are different, and most of the wavelengths can be found around 2350 nm and are therefore carbonates. The large amount of quartz in the thin sections could not be

observed during the hyperspectral analysis, as quartz does not have a spectral feature in the SWIR range.



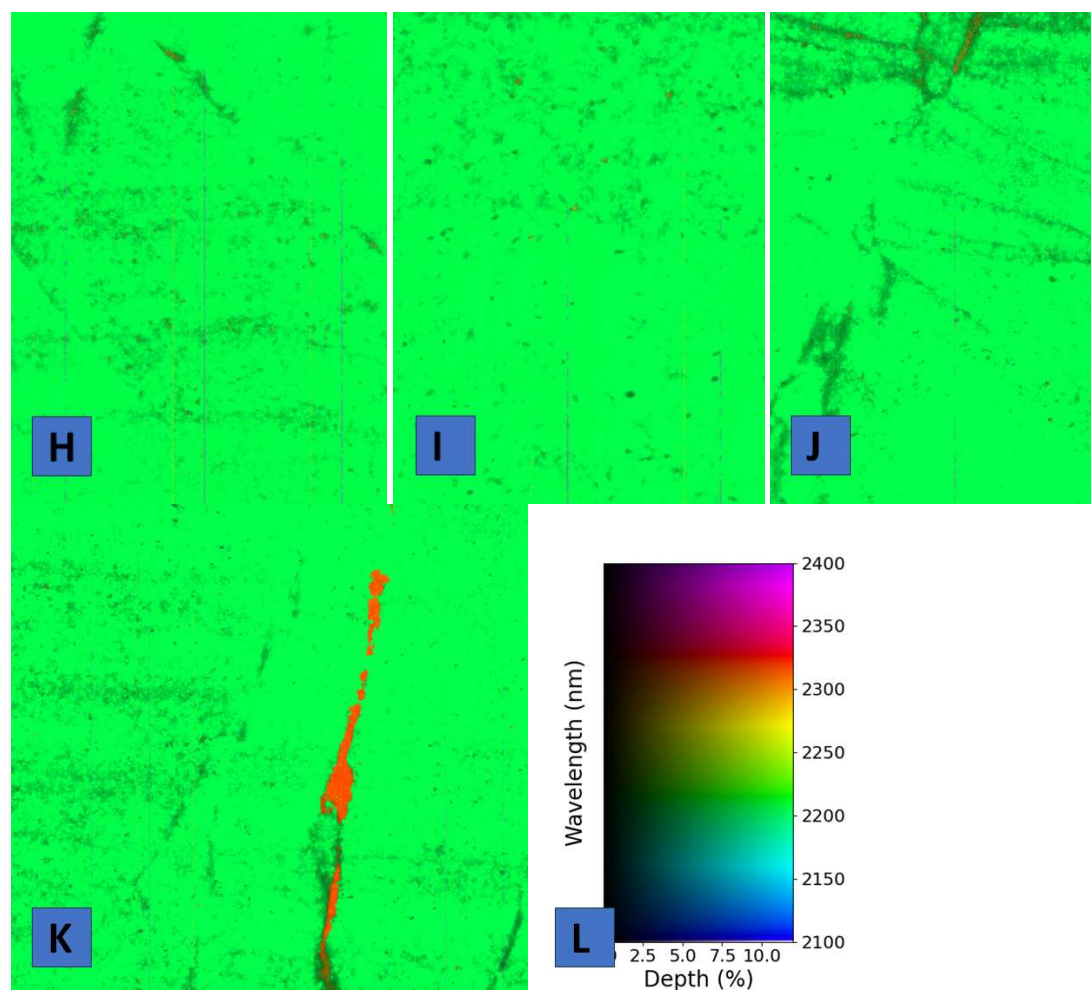


Figure 9: The different wavelengths maps with all pixels colored for all the 11 samples. A-K) Wavelength maps of the samples A-K. These are taken at about the same location as thin section 1-11 respectively. Most of the wavelengths are between 2200-2210 nm, related to phyllosilicates, but in sample 5, 6, 11 (E, F, K), the clear reddish color is indicative for the carbonate feature. L) The legend for sample 11; the colors for wavelength are the same for every figure, but the depth might vary as the applied depth stretch is not the same for every sample.

The ferrous drop ratio represents the ratio between the 1600 and the 1310 nm band and correlates to the amount of Fe^{2+} in the spectrum. These values do not significantly vary for the clays in the matrix and appear to be between about 1.0 and 1.4 (Appendix; Figure 2). Ferrous drop values that are greater than 1.4 in the matrix are all associated with ferroan dolomites. Specific layers in samples 8 and 10 show ferrous drops that are even lower than 1.0 and the fault surface, sample 7, shows the overall lowest values for the ferrous drop. Yet, also here, ferroan dolomites can be found. The largest iron drop values were found in the fault zones of the samples that were filled with dolomites and can reach values up to 3.0. The faults are easily distinguishable from the matrix as the ferrous drop is significantly higher in these. For sample 10, near and in the fault zone, not a lot of ferroan dolomites appear to be present. However, iron rich dolomites can be found in the specific layers around this fault zone (Appendix; Figure 2J).

The illite vs kaolinite value is calculated as the ratio between the value at 2195 nm divided by the value at 2178 nm. Steep slopes, that have a value greater than 1.0, are indicative for illite, while the shallow slopes, that are smaller than 1.0 indicate a large amount of kaolinite. As a result, the clay filled fractures have relatively low values, while towards the fracture zones, the illite vs kaolinite values are relatively high, indicative for larger amounts of illite. For the matrix, illite-rich layers are followed by kaolinite-rich layers (Appendix; Figure 4). On top of that, an offset in the fault zone in sample 11 (Appendix; Figure 4K) can be seen with the illite vs kaolinite ratio as bands with a high value show some clear offset with respect to each other. What further can be seen is that different types of kaolinite can be found in the matrix of the sandstones. For samples 4 and 5 (Appendix; Figure 4D, E), the illite vs kaolinite values appear to increase towards the fault zone that is filled with carbonates. Near the fault zone in thin section 6 (Appendix; Figure 4F), illite can be observed, while the fracture that is filled with clay and ends at the carbonate fault has very low values. In the matrix, the values for illite vs kaolinite vary significantly between approximately 0.875 until 1.05. These high illite vs kaolinite values can be found in the samples that correspond to the thin sections that show sedimentary structures. Sample 4 shows a clear boundary between relatively high and low values, with the clay fracture separating these two.

The illite crystallinity value is calculated as the ratio of the depth of the deepest feature observed within the 1850–2100 nm range divided by the depth of the deepest feature observed within the 2100–2400 nm range. The illite crystallinity maps show areas of grain comminution, such as deformation bands, with the places that have experienced more deformation related to the largest values. Illite crystallinity varies quite a bit throughout the matrix (Appendix; Figure 3). The illite crystallinity shows clear bands with more deformation, but also specific spots in the matrix of the sandstones where the illite crystallinity values are relatively large (Appendix; Figure 3J). Especially the matrix of sample 11 (Appendix; Figure 3K), shows a large increase in illite crystallinity when compared to the rest of the samples, while in sample 2 (Appendix; Figure 3B), the illite crystallinity values are, when compared to the rest of the samples, relatively small and remain the same throughout the matrix. Nevertheless, in here, a small fracture network can be seen

The analysis conducted via decision trees yields comprehensive insights into its mineralogical composition and fracture characteristics (Figure 10). The first feature decision tree makes a distinction between different pixels (Figure 10A). It identifies about 65% of the pixels as kaolinite, while it also suggests that about 28% of the sample is montmorillonite. This montmorillonite is the dominant phase where the clay-rich fracture is located. The remaining pixels are dolomite and calcite, with 1% determined to be other minerals. The molecular bond decision tree reveals kaolinite as the primary mineral constituent in both the matrix and clay-filled fractures (Figure 10B). About 90% of the sample is therefore kaolinite with the minerals determined in the carbonate fracture being (ferroan) dolomite, while the remaining 1% are other minerals, including a little bit of illite. The carbonates decision tree only looks at the carbonates present in the sample. As the previous decision trees already showed that kaolinite is present in large quantities, the decision tree determines that 96.3% of the pixels have no strong MgOH bond, while about 3.5% of the pixels are ferroan dolomite and the remaining part being other minerals, ankerite and dolomite in very small quantities (Figure 10C). The multiple aspect decision tree elucidates the predominant presence of kaolinite, about 60%, within the matrix, with mixtures of smectite and illite identified as the dominant material in and around the clay-rich fractures (Figure 10D). Additionally, the identification of ferroan dolomite in the carbonate-filled fracture zones is noted, with closer to these carbonates the presence of iron rich mixtures of smectite and illite.

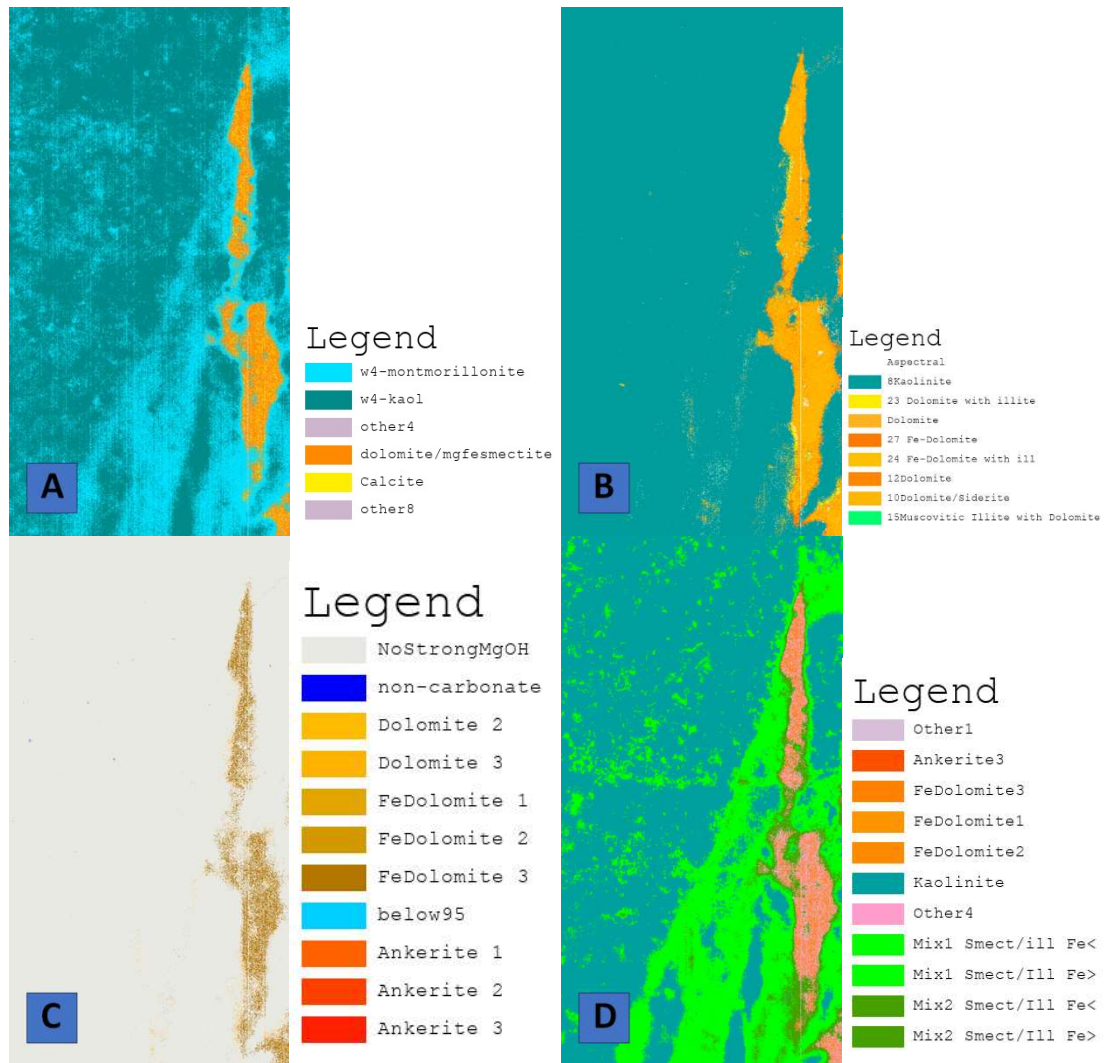


Figure 10: A): First feature decision tree. B): Molecular bond decision tree. C): Carbonate decision tree. D): Multiple aspect decision tree.

6.3 Matrix

The sandstone matrix consists of mostly quartz. As hyperspectral analysis cannot detect quartz nor feldspar, the values of the point counting analysis are therefore assumed to be the best representation of the matrix. The minerals identified in the matrix consist of detrital quartz, zircons, rutile, muscovite, and lithic fragments. The relative abundances of these minerals differ per thin section and do not show a correlation with depth (Appendix; Table 1). However, quartz is in all the samples the most abundant mineral present. The quartz grains in the matrix are broken up and fractured and the fractures are sometimes filled with secondary materials, including barite, while the quartz grains in close vicinity to the fault and fracture zones also show grain size reduction and cataclasis. The quartz grains show concavo-convex grain boundaries, while the porosity between these grains collapses. Not all the broken quartz grains are filled and therefore contain some porosity within them.

The secondary materials in the matrix are predominantly clays and dolomites. The clays that are found are illite, kaolinite, and based on the first feature decision tree

montmorillonite. For illite and montmorillonite, no evidence was found under the SEM and no evidence was found for montmorillonite with the optical light microscope, while the hyperspectral scanner suggests that illite is present in distinguishable quantities in at least various parts of some samples (Figure 11). Kaolinite emerges as the dominant clay mineral phase within the examined samples based upon optical microscopy and hyperspectral analysis (Appendix; Table 1; Figure 10B). Most of the pore-filling kaolinite appears as loosely arranged booklets, resulting in significant porosity between them (Figure 7C).

The dolomites vary in size and composition in the matrix and show very irregular forms (Figure 6B, 7B). The dolomites show cleavage planes that intersect at near right angles and appear to be equally spread over the matrix for each thin section when viewed with the optical light microscope. The dolomites in the matrix vary between non-ferroan dolomites to ferroan dolomites further towards the edges, as was seen with the SEM and the CCL, with a zone of dissolution on the edges of the non-ferroan dolomites. They contain contaminations of other elements, including magnesium and manganese. Iron concentrations in the ferroan dolomites can be up to approximately 5%, but the increase in iron content is not necessarily towards the outer edges. As seen with the SWIR, small areas with elevated iron levels are present in the matrix, these areas are, just as seen with the microscopes, irregularly divided over the matrix and are related to ferroan dolomites. These ferrous drop values are not as high as compared to the fault zones but are still remarkable features in the matrix.

Minerals that were found in minor quantities in the matrix of the Slochteren sandstone are muscovite grains, chlorite, rutile, barite, and zircons. Further, every thin section contains bitumen, which was found more often in specific layers and fractures.

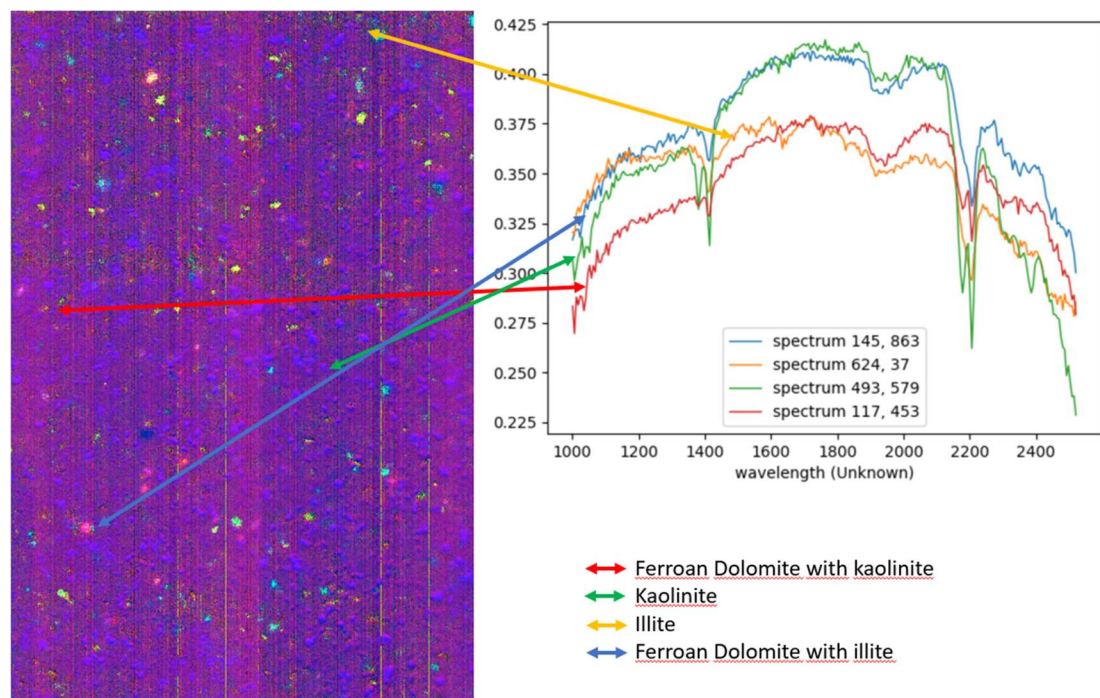


Figure 11: An overview of sample 9. It shows different types of ferroan dolomite in the matrix, each having a different ferrous drop. Further, the majority of the matrix consists of kaolinite, with some illite in between (blue patches).

6.4 Deformation structures

Three different deformation structures were identified in this study. The first one is a dolomite filled fault zone that can be found in thin sections 4, 5, 6, 10, and 11 that show some displacement. In the corresponding samples used for hyperspectral analysis, the dolomite-filled fault can be found in 5, 6, 11 and perhaps in 10. The second deformation structure primarily involves clay-filled deformation bands identified in thin sections 4, 5, and 6 and the same corresponding samples. The last deformation structures are bitumen filled fault zones, that show minor displacement and can only be clearly seen on thin sections 2 and 10.

The first deformation structure is a fault zone that was filled with several types of authigenic carbonates. In thin section 6, this identified fault zone was analyzed with the SEM. The minerals are identified as diverse types of ferroan dolomite, which exhibit notable deviations in iron content in the fault zone compared to the dolomites in the surrounding matrix, exceeding 15% of iron content. At least three different mineralogical compositions were determined with the SEM and the CCL. These dolomites have a small concentration of magnesium and manganese in them, and iron concentrations are significantly larger in the fault zone than in the matrix, while they show a chaotic pattern of fracture filling. The SWIR shows that the iron drop values throughout the fault zone can exceed 3.0 in samples 5, 6 and 11 (Appendix; Figure 2E, F, K), which is significantly higher than the iron drop values in the matrix, which only have a maximum of about 1.5. The iron drop values in sample 10 (Appendix; Figure 2J), the sample that might be related to the fault zone too, is not as high and only reaches about 2.4. What is further seen on the SWIR and the microscope is the sharp boundary between the fracture zone and the matrix. The hyperspectral analysis of sample 5 suggests that two sharp boundaries are present on both sides of the fault zone, while the microscopy analyses show a more gradual transitions on one side of the fracture. The fracture zone shows one edge with well cemented quartz grains in close vicinity to the fracture zone. Within these well cemented quartz grains, the grain size reduction is evident and the porosity between the quartz grains is collapsed. The detrital quartz grains in the fracture zone can be broken, and some minor porosity was found between them.

The second identified deformation structures involve clay-filled deformation bands identified in samples 5 and 6 (Figure 9E, F). These bands lack the distinct clear boundary observed in the carbonate-filled fracture and do not show displacement. Quartz grains within the deformation bands appear smaller and more angular compared to the surrounding matrix. Kaolinite predominates in these clay-filled fractures, detectable by their clear formed booklets (Figure 6F), although dolomite and quartz are also present in varying quantities. The ferrous drop in these fractures aligns with the matrix, while parameters such as illite crystallinity differ slightly. However, the clay-rich fractures can be clearly seen with the illite vs kaolinite ratio during hyperspectral analysis as the values are much lower than the surrounding matrix. The clayish-rich bands end when they reach the carbonate filled fracture zone. The almost complete porosity collapse in the carbonate filled fracture zone cannot be observed in this clayish-rich fracture zone, but the porosity is still smaller with respect to the matrix of the surrounding sandstones, with fracture porosity and vuggy porosity observable. These clay-filled rich fracture zones are boundaries for the illite vs kaolinite ratio as can be seen in sample 4 (Appendix; Figure 4D).

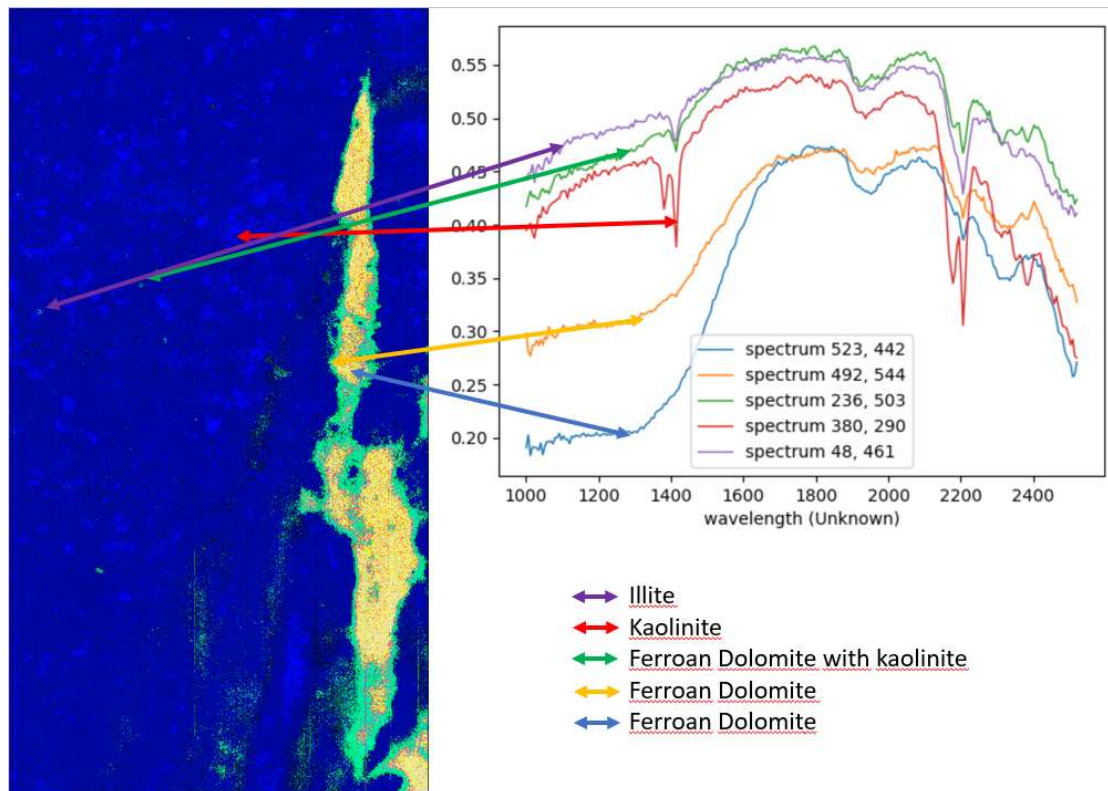


Figure 12: An overview of sample 6. It shows different types of ferroan dolomite in the fracture zone, each having a different ferrous drop. Ferroan dolomite is also present in the matrix, but the majority of the matrix consists of kaolinite, with some illite in between.

The last deformation structures comprise small bitumen-filled cracks within the sandstone, observable in thin sections 2 and 10, that show some minor displacement along parts of these fractures. Based on the hyperspectral analysis, these fractures can hardly be noticed, but show a minor increase in illite crystallinity. The fractures appear as slender within the sandstone matrix, often exhibiting jagged or irregular boundaries and typically range in width from micrometers to millimeters and are distributed sporadically throughout the rock. The illite crystallinity is slightly higher within these fractures, while the illite vs kaolinite ratio is relatively lower with respect to their surrounding matrix. These fractures do not show a clear indication of iron reduction as the iron drop is about equal to the surrounding materials. Grain size reduction of quartz grains is visible towards the fracture zone but is not as large as the carbonate or clay filled fracture zones.

7 Discussion

This study gives a detailed description of the mineralogy of fractures and their diagenesis in sandstone reservoirs, that were found in the K06-04 core, as they play a crucial role for hydrocarbon and fluid flow. Numerous Rotliegend fields exhibit compartmentalization due to faulting, which behave as barriers or conduits to fluid movement on both production and geological timescales, which influences the local fluid flow dynamics. As a result, hydrocarbon columns in Rotliegend fields can exceed expectations, because of fault sealing mechanisms (Ligtenberg et al., 2011). In this context, a detailed examination of fracture mineralogy, diagenesis, and characteristics is essential for refining fault properties and understanding the diverse mechanisms responsible for fluid flow. Techniques, including thin section analysis, scanning electron microscopy, cathodoluminescence microscopy, and hyperspectral imaging in the short-wave infrared region, have contributed to a further refining of the fault properties in the K06-04 core.

7.1 Comparison between the techniques

Four different techniques have been used throughout this study: the optical light, scanning electron, and cold cathodoluminescence microscopy as well as hyperspectral analysis (Table 4). All the different techniques have their own ad- and disadvantages and have been used to obtain the best possible mineralogical composition of structures found in the Slochteren sandstone.

7.1.1 Thin Section Analysis

The point counting was done on thin sections that were scanned under the optical light microscope. It offers high spatial resolution, allowing the observation of delicate details in rock textures and mineralogy. It allows the rapid identification of minerals, textures, and features such as cleavage, twinning, or zoning. The point counting provides quantitative data about the mineral composition of a rock sample. By counting the number, an estimation of the relative abundance of different minerals in the sample is determined. However, the thin section analysis is labor-intensive and time-consuming, especially for the samples with a fine-grained texture and there can be some subjectivity in mineral identification and counting, leading to potential variability. Misinterpretation of a specific mineral can therefore be evident. Over- or underestimation of a specific mineral group might be a consequence of this. On top of that, distinguishing between certain specific minerals (types of clay or dolomite) can sometimes be challenging (Savitri et al., 2021).

7.1.2 Scanning Electron Microscope

The SEM gives detailed topographical imaging and the versatile information garnered from different detectors. The instrument works fast and requires only minimal preparation actions. The SEM technique produces images with resolutions about ten times better than those obtained with the visible light microscope and can detect mineral components that are indistinguishable when using the light microscope. SEM can provide information on surface topography, crystalline structure, chemical composition, and electrical behavior of the top 10 micrometers of a specimen. With SEM, there is the possibility of getting more information than just the surface topography, e.g., crystal structure, chemical composition,

and electrical properties (Krinsley and Manley, 1989; Vernon-Parry, 1989). For SEM to work properly, the sample must be small and fit within the chamber size. This can limit the analysis of larger geological samples or require subsampling, potentially introducing sampling biases. In addition to imaging, SEM can provide elemental information through techniques such as energy-dispersive X-ray spectroscopy (EDS). However, interpreting elemental spectra requires expertise in understanding peak shapes, background noise, and potential spectral overlaps. If this is done wrong, misinterpretation of data will be a consequence (Kannan, 2018). Further, the making of mineral maps is a time-consuming process. To have maps with a good resolution, some considerable time is needed. On top of that, the purchase and maintenance of a SEM is, compared to the other techniques, significantly more expensive (Kannan, 2018). Lastly, the SEM cannot detect elements that are lighter than the carbon coating. Therefore, organic elements such as bitumen cannot be detected.

7.1.3 Cathodoluminescence

The cathodoluminescence microscope integrates petrographic and cathodoluminescence imaging, streamlining sample analysis for greater efficiency (Boggs and Krinsley, 2006). It provides a fast and interpretable overview of sample mineralogy, especially when combined with light microscopy. Specific minerals, including those with diverse compositions like dolomites that could not be identified with the optical light microscopy, can be rapidly identified under the cathodoluminescence microscope, benefiting from distinct luminescence properties. Additionally, cathodoluminescence imaging excels in highlighting intricate details of cement textures, crystal shapes, zoning patterns, and other textural features (Boggs and Krinsley, 2006). It enhances the visualization of mineral characteristics, enabling easy identification of minerals such as feldspar in specific regions. However, cathodoluminescence microscopy also has limitations. Variables such as color, intensity, and luminescence spectra are influenced by crystallographic orientation in thin sections (Walderhaug and Rykkje, 2000). Moreover, the need for customized settings for individual parts of thin sections makes the analysis time-consuming. Further, the high-energy beam emitted by the gun can induce sample damage or alterations, potentially compromising data reliability. Another disadvantage is the poorer resolution and magnification of images compared to those acquired when using the SEM (Boggs and Krinsley, 2006).

7.1.4 SWIR

Imaging spectrometry, simultaneous measurement of continuous spectra and images in up to hundreds of spectral channels or bands, is a proven technology for identifying and mapping minerals based on their reflectance or emissivity signatures (Kruse et al., 2012). The main benefit of the SWIR is that it is a fast way to obtain mineralogy from a core (Paradis et al., 2021). It offers a rapid, non-destructive method to determine mineralogy, while also providing compositional and textural information (McCormick et al., 2021). As a result, it gives a high spatial resolution dataset useful for analyzing mineralogy in cores (Kraal and Ayling, 2019). This work shows that hyperspectral imaging is an invaluable tool that reveals mineralogy, composition, and texture of carbonate rocks and clays. Nevertheless, care must be taken to consider the scale of observation, or spatial resolution, because each imaged pixel comprises several phases that contribute to the reflectance. The SWIR scanner determines spectral signatures of mixtures of specific minerals, making it sometimes difficult to distinguish between the minerals present. Only when minerals are large enough, the scanner shows unmixed spectral signatures. For host rock observations, under- or overestimations might therefore occur, and specific rare minerals determined with the optical light microscope and the SEM are not detected or overshadowed by quantities of

other minerals present. Therefore, the final percentages that have been determined with the decision trees vary significantly with respect to the thin section data percentage. Another drawback of the SWIR is that it cannot identify specific minerals present in sandstones. Not only quartz and feldspar cannot be distinguished as they do not show a diagnostic feature, but also heavy minerals that have been observed, such as barite and zircons cannot be identified with SWIR analysis (Kraal and Ayling, 2019; Hecker et al., 2019).

Given the distinct limitations inherent in the various identification methods, the selection of a technique should be based upon the specific research objectives. For instance, in situations where time is limited, methodologies such as hyperspectral scanning are preferred. However, when the focus is on the identification of feldspar and quartz, this technique becomes ineffective and other techniques are favored. Also, the availability of the thin sections must be considered. Should they be available, a combined approach utilizing optical light and cathodoluminescence microscopy should be enough to provide a first estimation of the mineralogical composition. Subsequently, SEM may be used for a more detailed analysis. Moreover, the scale of observation is also important; SEM proves the best for observing small scale minerals (> 20 micrometers), while the optical microscopes cannot zoom in that far, and the mixing in the data of the hyperspectral scanner makes it difficult to distinguish between these elements.

	Principle for mineral identification	Preparation needed	Results	Strengths	Limitations
Optical Light microscopy	Identification based on variety of optical properties (e.g. color pleochroism, refractive index, relief (Reedy, 1994)).	Thin sections need to be made; the sample is mounted on a glass slide using epoxy resin and then grounded to uniform thickness (Reedy, 1994)	<ul style="list-style-type: none"> - Relative abundance of different minerals. - Paragenesis. - Faults and Fractures. 	<ul style="list-style-type: none"> - Rapid identification of minerals, textures, and features 	<ul style="list-style-type: none"> - Labor-intensive and time consuming. - Misinterpretation of minerals due to variability. - Distinguishing between different minerals might be difficult (Nikonow et al., 2019).
Scanning electron microscopy	Focused beam of electrons produces compositional contrast (Krinsley and Manley, 1989)	Thin section needs to be coated.	<ul style="list-style-type: none"> - Surface topography - Crystal structure - Chemical composition (Kannan, 2018) 	<ul style="list-style-type: none"> - Much larger magnification than optical light microscope - Instrument works fast for specific points (Kannan, 2018). 	<ul style="list-style-type: none"> - Expertise necessary for identification of obtained spectra. - Biases due to limited sample analysis space. - Time consuming to make mineral maps. - Expensive apparatus.
Cold Cathodoluminescence microscopy	Emission of characteristic visible luminescence from specific substances (Boggs and Krinsley, 2006).	Same for optical light microscope.	<ul style="list-style-type: none"> - Details of cement textures, crystal shapes, zoning patterns, textural features (Boggs and Krinsley, 2006). 	<ul style="list-style-type: none"> - Greater efficiency due to combination of CCL and optical microscopy - Minerals that could not be identified with optical microscope can be with CCL. 	<ul style="list-style-type: none"> - Damage of sample if settings are not good. - Poorer resolution with respect to SEM.
Short wavelength infrared spectroscopy	Measuring and analysis of reflected electro-magnetic radiation in infrared wavelength ranges (Van Ruitenbeek et al., 2014).	Samples need to be clean and dry (Brouwer, 2022).	<ul style="list-style-type: none"> - Information about the mineralogical composition of a sample based on reflectance patterns. 	<ul style="list-style-type: none"> - Fast. - Nondestructive. - High spatial resolution. 	<ul style="list-style-type: none"> - Cannot determine minerals without an absorption feature in the SWIR range, such as quartz, feldspars, and garnets. (Hecker et al., 2019).

Table 4: Short comparison of mineralogical identification techniques. Table modified after Savitri et al., 2021.

7.2 Paragenesis

Several diagenetic stages were observed during the analyses. A relative paragenesis is proposed based on crosscutting microstructural relationships (Figure 13).

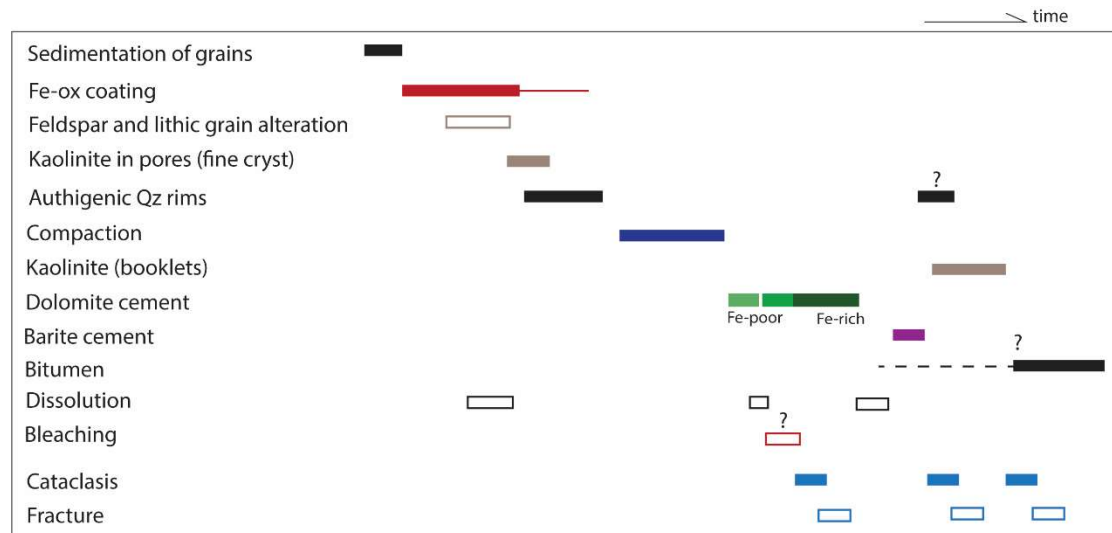


Figure 13: Proposed paragenetic sequence that is based on crosscutting microstructural relationships. Image credited to Eva de Boever.

The first phase of the paragenesis is characterized by grain-coating by iron oxi-hydroxides and during the eodiagenesis, at least part of the detrital quartz must have been fractured. This must have happened before the first phase of authigenic quartz rims have formed. The authigenic quartz is probably derived from the excess silica liberated during feldspar dissolution (Rossel, 1982). By the end of the eodiagenesis, complete dissolution of feldspars is expected as no evidence was found for feldspar with CCL and SEM analysis. The feldspar must have been dissolved when it came into contact with CO₂ rich fluids that satisfy the conditions for kaolinite precipitation and quartz overgrowths (Lanson et al., 2002). As a result, the feldspar content in the thin sections appears to be neglectable. However, traces of feldspar elements could be found in the kaolinite booklets, as shown with the SEM, as the kaolinite minerals had some traces of Na and K in them, suggesting that alkali feldspars were present, which is in line with other studies that still can find feldspar in similar cores from the Rotliegend (Miocic et al., 2020; Gluyas et al., 1997).

After the compaction of the sandstone occurred during the early stages of the burial, the first non-ferroan dolomites must have formed. This must have happened prior to the Jurassic uplift according to Miocic et al. (2020). The non-ferroan precipitation is interpreted according to Vincent et al. (2018) as a precipitate from saline brines migrating downwards from the Zechstein. This downward migration of the saline brines must have stopped, as a minor phase of dissolution took place that explains the dissolute rims that can be found in the non-ferroan dolomites. The fluids must have become iron rich, possibly fluids from the Carboniferous Coal Measures, that migrated upwards, with the non-ferroan dolomite serving as nucleating sites for the ferroan dolomite (Miocic et al. 2020). After the first ferroan precipitation took place, the carbonate fault zone must have formed, which was a conduit for the upward migrating fluids from the Carboniferous Coal Measures (Rossel, 1982). The dolomite cement became increasingly iron-rich when diagenesis progressed, in line with Bukar et al.

(2021) and Ziegler (2006). The timing for this is according to Vincent et al. (2018) during the Mid Cimmerian Unconformity. The faulting and fracturing allowed the upward migration of even more CO₂-bearing, acidic and reducing, hotter fluids from the Carboniferous. This might be an explanation for the large differences in iron content between the ferroan dolomite in the matrix and the ferroan dolomite in the fracture zone. According to Ziegler (2006), the late burial stages are represented by ankerite precipitation, as ankerite represents the final phase of carbonate precipitation. Ankerite could not be confirmed in the samples investigated here.

After that, another phase of authigenic quartz caused a second phase of quartz rimming, which occurs as relatively large overgrowths. Kaolinite booklets must have formed during this phase as they are intimately associated with the quartz overgrowths. Kaolinite is also the filling material of the second fracture phase, which ends at the carbonate filled fracture. These kaolinite booklets have a relatively low illite vs kaolinite ratio and a relatively low illite crystallinity. Ergo, based on the reflectance spectra, the clay in the fault should be kaolinite, while the illite vs kaolinite ratio suggests that illite is present more towards the fault zone. However, the SEM and the optical light microscope do not show any evidence for illite present in or near the dolomite filled fault zone. At best, kaolinite clays with some minor contaminations of illite. The formation of the kaolinite in the fractures most likely occurred during the Cretaceous (Gauthier et al., 2000), but evidence for this is missing, which could also not be substantiated during this study.

At the final stage, bitumen must have been formed, in agreement with Vincent et al. (2018). As can be seen in thin section 7, the bitumen sometimes forms around the grains or might break the grains. The bitumen is also present in slender fractures, such as the one found in thin section 2 and in specific bands in the matrix.

7.3 Structural analysis.

The structural analysis of the K06-04 core reveals a complex interplay of geological features that provide insights into the structural evolution and reservoir characteristics of a part of the sedimentary sequence in the lower Slochteren member. At least three different deformation structures were found during this study, with fracture networks in the K06-04 core relatively complex, similar to Robertson et al. (2023) (Figure 14). Gauthier et al. (2000) also showed that different fractures can be identified in the broad fourteens basin, at about the place where the K06-04 core is located.

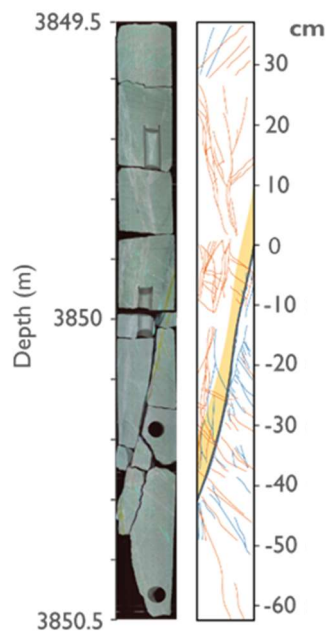


Figure 14: Complex deformation network in the K06-04 core. The main fault zone, that is filled with ferroan dolomites, is colored yellow and corresponds to thin section 4, 5, 6.

The main fault zone is captured in thin sections 4, 5, and 6 and in samples 5 and 6. The ferroan dolomite that filled the fault in thin section 11 is, because of the same values for ferrous drop, possible filled with the same material and during the same time as the fault zone in thin sections 4, 5, and 6. As can be seen on the ferrous drop from the samples from this study (Appendix; Figure 2), as well as on the whole K06-04 core (Figure 15), which show that the values of the fault zone (around 3850 m) are very similar to the values found in thin section 11 (around 3853 m). Because of the deviations that might be associated with the drilling of the core, it is difficult to say if the fault continues all the way to thin section 11, or if an alternative explanation, e.g. a Riedel shear, is a more straightforward explanation.

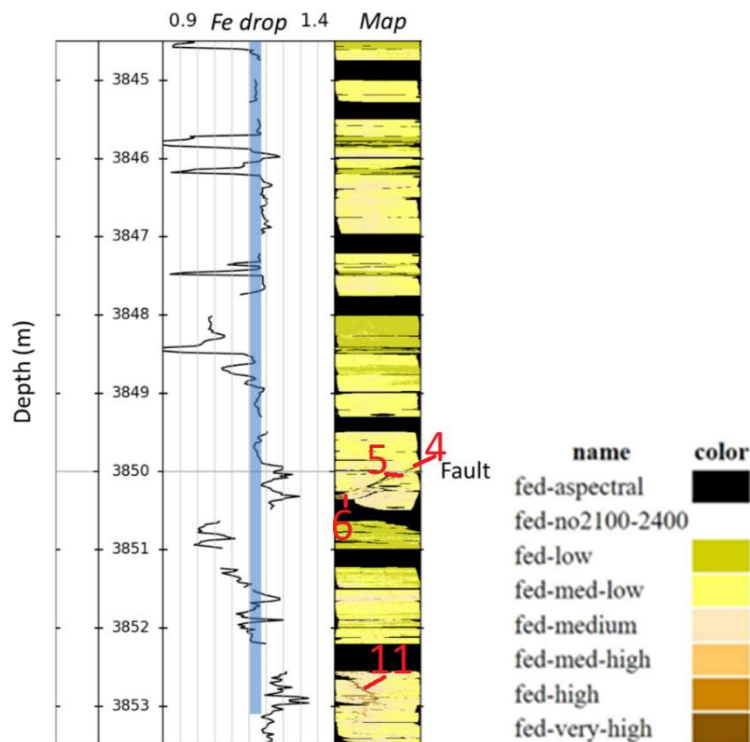


Figure 15: Ferrous drop as determined by Robertson et al. (2023). The location of thin sections 4, 5, 6, and 11 are indicated. Ferrous drop appears to be the same in every location, similar to the results from this study. Note: sample 4 of this study is not taken in the dolomite fault zone and therefore does not contain iron (Appendix; Figure 2D).

Sample 10 shows a high degree of illite crystallinity and is taken at approximately 3851.5 meter depth. This sample shows a fault zone, that has a couple centimeters of displacement and appears to be filled with dolomite based on thin section analysis, but the iron drops are very low when compared to the main fault zone. It is therefore suggested that it is filled with non-ferroan dolomite. Yet, some smaller iron drop values are present around this fault zone, but the maximum values in this part do not correspond to the relatively high iron drops found in the samples from the main fault zone. Explanation might be related to a different fault phase, that occurred before the main fault as is suggested by Gauthier et al. (2013). The second fracture event in Gauthier et al. (2013) is related to cataclastic shears and is filled with Fe-dolomite and siderite cements formed during the main burial, which is very similar to the Fe-dolomite filled fault zone found in this study. However, more research is needed to substantiate this.

The fault zone filled with ferroan dolomite is characterized by grinding of the quartz grains after which cataclasis took place. The fault must have acted as a conduit, and through the fault zone, iron-rich fluids must have flowed, after which the ferroan dolomites filled the fault, decreasing the porosity inside it. Evidence for grinding and cataclasis is also given in similar studies in the Rotliegend (Van Hulten, 2010; Gauthier et al., 2000). The cataclasis was seen around all the thin sections that included the main fault zone. This might be a possible reason that the Slochteren Formation was capable of trapping hydrocarbons (Ligtenberg, 2011), which is contrary to Gauthier et al. (2000), who suggest that the carbonates from the Zechstein are the minerals that are responsible for the trapping. However, both authors agree that the porosity is decreased towards fault zone, which is similar to the results from the K06-04 core. Van Hulten (2010) suggests that carbonate cements are often very patchy

in faults seen in cores. This might explain why the carbonates cannot be found with the hyperspectral along the complete fault zone and be a reason for the varying ferrous drops, as in certain places in sample 5 and 6, clear regions with an overall larger amount of iron can be seen. Especially in sample 6, the carbonates are not interconnected. If this is the case, it is highly unlikely that the carbonate fault zone was the reason for the trapping of the hydrocarbons. However, it is difficult to say if the complete fault zone is present in the sample. Furthermore, the dolomites observed on the thin sections do seem to connect.

The second deformation structure that has been determined are fractures that end on the carbonate fault and are filled with kaolinite. No displacement has been seen, but it cannot be ruled out that some displacement is present. The illite crystallinity shows that the majority of the clay filled faults have a low illite vs kaolinite ratio, while the clay that surrounds the carbonate fault has a relatively high ratio. Distinction between the two different types of clay can be seen on sample 4 (Appendix; Figure 4D), where the places with the low illite vs kaolinite ratio correspond to the places with the low illite crystallinity, which contrasts with the illite crystallinity values in sample 10 but is similar to what is found in Robertson et al. (2023). Other studies have not seen fracture fillings with clay, but suggest, based on data from shallower depths, that the fracture event after the ferroan dolomite filled fault zone must have been filled with anhydrite cements (Gauthier et al., 2000; McNeil et al., 1998; Vincent et al., 2018). No evidence for the presence of anhydrite in the K06-04 core is found. The porosity distribution in the kaolinite filled fractures is generally larger than found in the carbonate filled fracture, while smaller than in the matrix. However, similarly to Gaupe et al. (1993), the fractures found have decreased the porosity.

The bitumen filled deformation structure does not show a high degree of illite crystallinity, while it appears to be a fault zone with some minor displacement. Bitumen in these fractures has not been identified during the hyperspectral scanning. Bitumen deposits have been found (Vincent et al., 2018) and have been found in the Slochteren sandstone at similar depth (Schmidt et al., 2000), but no evidence for faults associated with this bitumen is found.

7.4 Reservoir Quality

The fractures greatly influenced the porosity, not only because the quartz grains near the fault zone broke apart, crumbled and were mechanically compacted, but also because the fracture operated as a conduit for fluid flow, causing the deposition of carbonates along the fault and significantly reducing the porosity and permeability. The effect of fluid flow, from the underlying Carboniferous and overlying Zechstein, is not easy to quantify, yet plays an important role as it had a large influence on the carbonate cementation and associated porosity loss (Busch et al., 2020). Because of the porosity collapse, the ferroan dolomite filled fault zone appears to behave as a barrier to fluid flow when CO₂ will be injected and it is unlikely for fluids to migrate through the dolomites, nor for the fault to become seismic active. However, field scale experiments have shown that leakage might take place in reservoirs with carbonate cap rocks by activation of the fault, despite being minimal, when injecting CO₂ (Guglielmi et al., 2021). The rupture of the fault itself happened aseismic, but associated problems with these earthquakes are that they might damage the seal integrity and potentially cause leakage (Zoback et al., 2012). As these earthquakes happen in most cases aseismic, using seismicity is difficult to estimate the integrity of the caprock (Guglielmi et al., 2021). However, according to Vilarrasa and Carrera (2015), fault reactivation is unlikely related to the leakage of CO₂ as caprocks contain high contents of clay, which ensures a reduced permeability and raises the entry pressure within the confined deformation zone.

During this study, the true amount and presence of illite remains difficult to determine as different methods contradict each other. Illite appears to be present in specific layers or in close proximity to the fault zone according to hyperspectral analysis, but this has not been substantiated with other techniques. However, assuming that it is present, then the type of illite is important at the depth of the K06-04 core (Ramm and Ryseth, 1996). Two types of illite need to be considered for an estimation of the reservoir quality: the pore lining illite and the pore filling, bridging fibrous type (Seemann, 1979; Van Hulten, 2006). The growth of fibrous illite is of importance because it has a negative impact on permeability, while the bridging illite, especially the fibrous, hairy type, strongly reduces the permeability as well (Seemann, 1979; Ramm and Ryseth, 1996; Van Hulten, 2006). But, because not a significant amount of illite has been determined during the microscopy analyses, more research is needed to accurately determine the illite factor for porosity and permeability reduction.

7.5 Recommendations

Thin sections and scanned samples are not taken at the exact same location. Between the sample and the thin section, an offset of at least a couple of millimeters was present. This might not have a considerable influence on the host mineral composition, however, as characteristic features have been selected for the thin sections, a difference between the thin section and the scanned sample is observable. It explains for example why the top of the carbonate fracture in thin section 4 could not be identified during the hyperspectral analysis. In these cases, it cannot be substantiated if the mineralogy of the fault is indeed correctly identified. Recommended is therefore to make first hyperspectral scans, after which thin section should be made at the same location.

The hyperspectral scanner can only regard the minerals spectral active in the short wavelength infrared region. As a result, it overestimates the amounts of clay and carbonates significantly with respect to the quartz and potential feldspar content that are present in cores from the Slochteren. It can therefore be useful to explore more regions of the electromagnetic spectrum to obtain better estimates of the mineralogy. For the identification of quartz and feldspars, LWIR might help as this range of the infrared spectrum can detect these minerals (Figure 16). Drawbacks are related to the fact that LWIR is more difficult to interpret than SWIR because many combinations are non-unique and that LWIR and SWIR still cannot record all the different minerals that can be present in Slochteren sandstones (Kraal et al., 2019). Hence, this might only be a partial solution.

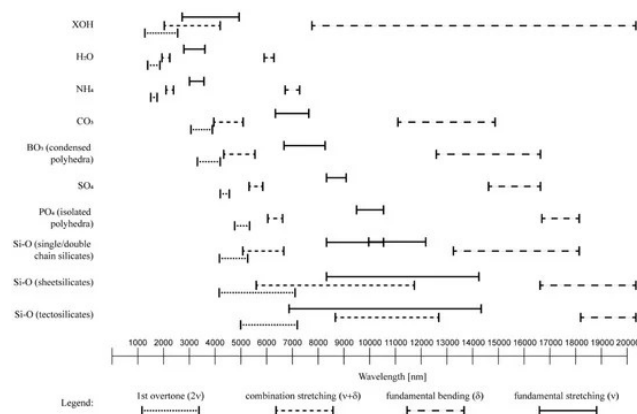


Figure 16: Different bonds that can be detected during hyperspectral analysis. LWIR (>3000 nm) is needed for the determination of quartz and feldspar. Figure from Laukamp et al. (2021)

Another recommendation is not to take the illite vs kaolinite ratio at two specific places (in this report at the bands 2195 and 2178), as the bands can vary throughout the core but also in the sample itself (Appendix; Figure 4). Different types of kaolinite appear to be present in the sample but are wrongly interpreted due to their (slightly) different position of bands (Figure 17). As a result, the slope of illite vs kaolinite is increased and illite is overestimated during the hyperspectral analysis. One of this examples is in sample 10, where the fault zone shows a high degree of illite vs kaolinite. However, when the spectra are analyzed, the doublet feature corresponding to kaolinite can be observed. To improve upon this problem, it is recommended to determine the peak after the trough at around 2200 nanometer. If this is done, the doublet feature will be determined and the amount of illite will not be overestimated. With this in mind, it is expected that the assumptions that the amount of illite increases towards the fault zone might possibly not be completely accurate as doublet features can be recognized. Rather, a different type of kaolinite, that has a different spectrum, is present near the fault zone. This might also explain why montmorillonite is determined in the first feature decision tree as the ratio between the clays varies throughout the core. Determining clays based on ratios is therefore sensitive to misinterpretation.

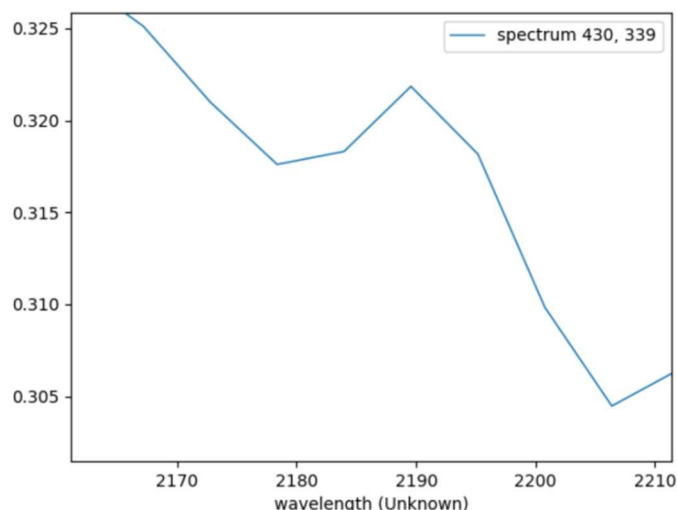


Figure 17: Spectrum of a pixel in the fault zone in sample 10. It shows the doublet feature, indicative for kaolinite. However, as the illite vs kaolinite ratio is determined at the wavelengths of 2195 and 2178, a steep slope is calculated, indicative for illite.

This study demonstrates that the combination of optical light microscopy (and thin section analysis), with SEM, cathodoluminescence, and hyperspectral analysis shows potential for future research. The benefit of merging the four different methods is that they all contribute in a different way to the result, as all the techniques have their own limitations that are being compensated for by at least one of the others. It is therefore recommended for future studies to take advantage of the imaging strengths offered by the combination of the techniques whenever feasible. If this is not possible, a choice of the best methods suited for the main aim should be chosen.

8 Conclusion

The Rotliegend sandstones that have been found in the K06-04 core consist out of detrital amounts of quartz, zircons, rutile, muscovite, and lithic grains. The authigenic minerals consist primarily out of clay and (non-)ferroan dolomite, with some barite as well. The clays and (non-)ferroan dolomites are present in the matrix itself but are also a large component in the fractures that have been found. Also, bitumen was found in the matrix, as well as in slender fractures. Further, some significant porosity differences between the different thin sections are observable. However, no link with depth can be established. Within the fractures, porosity and permeability is reduced with respect to its surroundings.

Three different deformation structures were observed, all associated with grinding and a strong reduction in grain size. The first is related to a fault zone with, based on SEM, CL, and SWIR analysis, different types of ferroan dolomites that can possibly be found on multiple places in the core. The first phase of fractures is completely filled with several types of ferroan dolomite and has an almost complete porosity collapse. The filling of the fracture is interpreted to have taken place in the earlier stages of the diagenetic sequence. The second fracture phase is filled with kaolinite. This fracture has a higher porosity when compared to the first fracture phase, but still less than the matrix and ends on the carbonate filled fracture. The third is a small fault zone, only visible on a small scale, shows minor displacement and is filled with bitumen.

The feldspars, that were present in the K06-04 core appear to have been completely dissolved. Remains of these feldspar grains can be found in some kaolinites but are relatively rare. The dissolution, that took place before the first fractures formed in the sandstone, must have occurred at a local scale, and might explain why the K06-04 core does not contain any feldspar (anymore), while similar other cores from the Rotliegend still have small percentages of feldspar in them.

The different techniques used for the identification of minerals in the core all have their strengths and weaknesses. It is important to consider for what purpose the technique is proven to be the best. Cathodoluminescence is a good technique for mineral identification because it provides valuable insights into the composition, texture, and crystalline structure of minerals. Short wavelength infrared is a valuable tool for the identification of carbonate and clay minerals in sandstones, as it cannot identify quartz and feldspar. Yet, important observations with respect to the clay and carbonate minerals in the fractures were made. The SWIR hyperspectral imaging has the capacity to detect nuanced diagenetic variations within these clayish and carbonate rocks and is compared to the other methods very fast. The scanning electron microscope is a powerful technique for mineral identification due to its ability to produce high-resolution images and detect elemental composition, providing detailed information about surface topography, crystalline structure, and chemical composition of minerals at the microscale, while the point counting combined with optical light microscopy is a valuable technique for mineral identification and quantification in rock samples, offering high spatial resolution and allowing identification of minerals and textures through analysis of mineral composition based on point counts. When multiple of the aforementioned methods are used, a coherent interpretation of the Rotliegend sandstones can be made.

9 References

- Amthor, J. E., & Okkerman, J. (1998). Influence of early diagenesis on reservoir quality of Rotliegende sandstones, northern Netherlands. *AAPG bulletin*, 82(12), 2246-2265.
- Angeli, M., Soldal, M., Skurtveit, E., & Aker, E. (2009). Experimental percolation of supercritical CO₂ through a caprock. *Energy Procedia*, 1(1), 3351-3358.
- Bakker, W. (2012). Hyperspectral Python. Retrieved from [Hyperspectral Python \(is-great.org\)](https://is-great.org)
- Balson, P., Butcher, A., Holmes, R., Johnson, H., Lewis, M., & Musson, R. (2002). North Sea Geology (Technical Report). British Geological Survey.
- Bense, V. F., & Person, M. A. (2006). Faults as conduit-barrier systems to fluid flow in siliciclastic sedimentary aquifers. *Water Resources Research*, 42(5).
- Birkholzer, J. T., Oldenburg, C. M., & Zhou, Q. (2015). CO₂ migration and pressure evolution in deep saline aquifers. *International Journal of Greenhouse Gas Control*, 40, 203-220.
- Bjørlykke, K. (2006). Effects of compaction processes on stresses, faults, and fluid flow in sedimentary basins: examples from the Norwegian margin. Geological Society, London, Special Publications, 253(1), 359-379.
- Bjørlykke, K., & Høeg, K. (1997). Effects of burial diagenesis on stresses, compaction and fluid flow in sedimentary basins. *Marine and Petroleum Geology*, 14(3), 267-276.
- Boldy, S. A. R., & Brealey, S. (1990). Timing, nature and sedimentary result of Jurassic tectonism in the Outer Moray Firth. Geological Society, London, Special Publications, 55(1), 259-279.
- Boukary, M., Worden, R. H., Bukar, S., & Shell, P. (2021). Diagenesis and its controls on reservoir quality of the Tambar oil field, Norwegian North Sea. *Energy Geoscience*, 2(1), 10-31.
- Brouwer, G. C. (1972). The Rotliegend in the Netherlands. *Rotliegend, Essays on European Lower Permian*. EJ Brill (Leiden), 34-42.
- Brouwer, M. (2022). Relationships between the physical properties of Triassic sandstones in the West Netherlands Basin and short-wave infrared reflectance spectroscopy (Unpublished master's thesis). Utrecht University.
- Busch, B., Hilgers, C., & Adelmann, D. (2020). Reservoir quality controls on Rotliegend fluvio-aeolian wells in Germany and the Netherlands, Southern Permian Basin—Impact of grain coatings and cements. *Marine and Petroleum Geology*, 112, 104075.
- Choquette, P. W., & Pray, L. C. (1970). Geologic nomenclature and classification of porosity in sedimentary carbonates. *AAPG bulletin*, 54(2), 207-250.

De Jager, J., & Visser, C. (2017). Geology of the Groningen field—an overview. *Netherlands Journal of Geosciences*, 96(5), s3-s15.

De Jager, J. & Geluk, M. (2007). Petroleum Geology. From: Geology of the Netherlands. Edited by Th.E. Wong, D.A.J. Batjes & J. de Jager, Royal Netherlands Academy of Arts and Sciences, 2007: 241–264.

De Lugt, I. R., Van Wees, J. D., & Wong, T. E. (2003). The tectonic evolution of the southern Dutch North Sea during the Paleogene: basin inversion in distinct pulses. *Tectonophysics*, 373(1-4), 141-159.

Ebbing, J., & Olesen, O. (2010). New compilation of top basement and basement thickness for the Norwegian continental shelf reveals the segmentation of the passive margin system. In *Geological Society, London, Petroleum Geology Conference Series* (Vol. 7, No. 1, pp. 885-897). London: The Geological Society of London.

Eftekhari, A. A. (2021). A thermodynamic and technical feasibility study of subsurface storage of energy in the North Sea abandoned reservoirs. In *34th International Conference on Efficiency, Cost, Optimization, Simulation and Environmental Impact of Energy Systems*.

Fazlikhani, H., Fossen, H., Gawthorpe, R. L., Faleide, J. I., & Bell, R. E. (2017). Basement structure and its influence on the structural configuration of the northern North Sea rift. *Tectonics*, 36(6), 1151-1177.

Fisher, M. J., & Miles, J. A. (1983). Kerogen types, organic maturation and hydrocarbon occurrences in the Moray Firth and South Viking Graben, North Sea basin. *Geological Society, London, Special Publications*, 12(1), 195-201.

Gauthier, B. D. M., Franssen, R. C. W. M., & Drei, S. (2000). Fracture networks in Rotliegend gas reservoirs of the Dutch offshore: implications for reservoir behaviour. *Netherlands Journal of Geosciences*, 79(1), 45-57.

Glennie, K. W., & Provan, D. M. J. (1990). Lower Permian Rotliegend reservoir of the southern North Sea gas province. *Geological Society, London, Special Publications*, 50(1), 399-416.
Glennie, K. W. (1997). Recent advances in understanding the southern North Sea Basin: a summary. *Geological Society, London, Special Publications*, 123(1), 17-29.

Glennie, K. W. (1972). Permian Rotliegendes of northwest Europe interpreted in light of modern desert sedimentation studies. *AAPG Bulletin*, 56(6), 1048-1071.

Gluyas, J., Jolley, L., & Primmer, T. (1997). Element mobility during diagenesis: sulphate cementation of Rotliegend sandstones, Southern North Sea. *Marine and Petroleum Geology*, 14(7-8), 1001-1011.

Guglielmi, Y., Nussbaum, C., Cappa, F., De Barros, L., Rutqvist, J., & Birkholzer, J. (2021). Field-scale fault reactivation experiments by fluid injection highlight aseismic leakage in caprock analogs: Implications for CO₂ sequestration. *International Journal of Greenhouse Gas Control*, 111, 103471.

Hallam, A. (1971). Mesozoic geology and the opening of the North Atlantic. *The Journal of Geology*, 79(2), 129-157.

Hecker, C., van Ruitenbeek, F. J., Bakker, W. H., Fagbohun, B. J., Riley, D., van der Werff, H. M., & van der Meer, F. D. (2019). Mapping the wavelength position of mineral features in hyperspectral thermal infrared data. *International Journal of Applied Earth Observation and Geoinformation*, 79, 133-140.

Hecker, C., van Ruitenbeek, F. J., Bakker, W. H., Fagbohun, B. J., Riley, D., van der Werff, H. M., & van der Meer, F. D. (2019). Mapping the wavelength position of mineral features in hyperspectral thermal infrared data. *International Journal of Applied Earth Observation and Geoinformation*, 79, 133-140.

Huang, J., Chen, H., Han, J., Deng, X., Lu, W., & Zhu, R. (2018). Alteration zonation and short wavelength infrared (SWIR) characteristics of the Honghai VMS Cu-Zn deposit, Eastern Tianshan, NW China. *Ore Geology Reviews*, 100, 263-279.

Kannan, M. (2018). Scanning electron microscopy: Principle, components and applications. A textbook on fundamentals and applications of nanotechnology, 81-92.

Kent, P. E. (1975). Review of North Sea basin development. *Journal of the Geological Society*, 131(5), 435-468.

Kolyukhin, D., Schueller, S., Espedal, M. S., & Fossen, H. (2010). Deformation band populations in fault damage zone—impact on fluid flow. *Computational Geosciences*, 14, 231-248.

Kraal, K. O., & Ayling, B. (2019, February). Hyperspectral characterization of fallon FORGE Well 21-31: New data and technology applications. In *Proceedings, 44th Workshop on Geothermal Reservoir Engineering* (No. 2016, pp. 1-15).

Krinsley, D. H., & Manley, C. R. (1989). Backscattered electron microscopy as an advanced technique in petrography. *Journal of Geological Education*, 37(3), 202-210.

Kruse, F. A. (2015). Integrated visible and near-infrared, shortwave infrared, and longwave infrared full-range hyperspectral data analysis for geologic mapping. *Journal of Applied Remote Sensing*, 9(1), 096005-096005.

Lanson, B., Beaufort, D., Berger, G., Bauer, A., Cassagnabere, A., & Meunier, A. (2002). Authigenic kaolin and illitic minerals during burial diagenesis of sandstones: a review. *Clay minerals*, 37(1), 1-22.

Larsen, O. (1971). K/Ar Age Determinations from the Precambrian of Denmark.

Laukamp, C., Rodger, A., LeGras, M., Lampinen, H., Lau, I. C., Pejčic, B., Stromberg, J., Francis, N. & Ramanaidou, E. (2021). Mineral physicochemistry underlying feature-based extraction of mineral abundance and composition from shortwave, mid and thermal infrared reflectance spectra. *Minerals*, 11(4), 347.

Laukamp, C., Rodger, A., LeGras, M., Lampinen, H., Lau, I. C., Pejčic, B., ... & Ramanaidou, E. (2021). Mineral physicochemistry underlying feature-based extraction of mineral abundance and composition from shortwave, mid and thermal infrared reflectance spectra. *Minerals*, 11(4), 347.

Ligtenberg, H., Okkerman, J., & De Keijzer, M. (2011). Fractures in the Dutch Rotliegend—An Overview.

Manda, U., Mazumdar, S., & Peles, Y. (2024). Effects of buoyancy in a laminar flow of supercritical carbon dioxide in a horizontal microchannel at different gravities. *International Communications in Heat and Mass Transfer*, 150, 107195.

McCormick, C. A., Corlett, H., Stacey, J., Hollis, C., Feng, J., Rivard, B., & Omma, J. E. (2021). Shortwave infrared hyperspectral imaging as a novel method to elucidate multi-phase dolomitization, recrystallization, and cementation in carbonate sedimentary rocks. *Scientific Reports*, 11(1), 21732.

McNeil, B., Shaw, H. F., & Rankin, A. H. (1998). The timing of cementation in the Rotliegend sandstones of the Southern North Sea: A petrological and fluid inclusion study of cements. *Journal of Petroleum Geology*, 21(3), 311-327.

Mazzullo, S. J. (2004). Overview of porosity evolution in carbonate reservoirs. *Kansas Geological Society Bulletin*, 79(1-2), 1-19.

Metz, B., Davidson, O., De Coninck, H. C., Loos, M., & Meyer, L. (2005). IPCC special report on carbon dioxide capture and storage. Cambridge: Cambridge University Press.

Miocic, J. M., Girard, J. P., Schoener, R., & Gaupp, R. (2020). Mudstone/sandstone ratio control on carbonate cementation and reservoir quality in Upper Permian Rotliegend sandstones, offshore the Netherlands. *Marine and Petroleum Geology*, 115, 104293.

Nicol, A., Seebeck, H., Field, B., McNamara, D., Childs, C., Craig, J., & Rolland, A. (2017). Fault permeability and CO₂ storage. *Energy Procedia*, 114, 3229-3236.

Nikonow, W., Rammlmair, D., Meima, J. A., & Schodlok, M. C. (2019). Advanced mineral characterization and petrographic analysis by μ -EDXRF, LIBS, HSI and hyperspectral data merging. *Mineralogy and Petrology*, 113, 417-431.

NLOG Mapviewer. (2024). Retrieved from <https://www.nlog.nl/nlog-mapviewer/brh/106528321?lang=nl>

NV5 Geospatial Solutions, Inc. (2024). ENVI. Retrieved from <https://www.nv5geospatialsoftware.com/>

Özmaral, A., Abegunrin, A., Keil, H., Hepp, D. A., Schwenk, T., Lantzsich, H., ... & Spiess, V. (2022). The Elbe Palaeovalley: Evolution from an ice-marginal valley to a sedimentary trap (SE North Sea). *Quaternary Science Reviews*, 282, 107453.

Paradis, M. C. M., Doucet, F. R., Rifai, K., Özcan, L. Ç., Azami, N., & Vidal, F. (2021). ECORE: A new fast automated quantitative mineral and elemental core scanner. *Minerals*, 11(8), 859.

Petrie, E. S., Petrie, R. A., & Evans, J. P. (2014). Identification of reactivation and increased permeability associated with a fault damage zone using a multidisciplinary approach. *Journal of Structural Geology*, 59, 37-49.

Pharaoh, T., England, R., & Lee, M. (1995). The concealed Caledonide basement of eastern England and the southern North Sea—a review. *Studia geophysica et geodaetica*, 39, 330-346.

- Ramm, M., & Ryseth, A. E. (1996). Reservoir quality and burial diagenesis in the Statfjord Formation, North Sea. *Petroleum Geoscience*, 2(4), 313-324.
- Rasmussen, E. S. (2009). Neogene inversion of the central Graben and Ringkøbing-Fyn high, Denmark. *Tectonophysics*, 465(1-4), 84-97.
- Rasmussen, E. S., & Dybkjær, K. (2020). The lower Miocene flint conglomerate, Jylland, Denmark: a result of the Savian tectonic phase. *GEUS Bulletin*.
- Rasmussen, L. B. (1974). Some geological results from the first five Danish exploration wells in the North Sea. I kommission hos CA Reitzels Forlag.
- Rattee, R. P., & Hayward, A. B. (1993). Sequence stratigraphy of a failed rift system: the Middle Jurassic to Early Cretaceous basin evolution of the Central and Northern North Sea. In *Geological Society, London, Petroleum Geology Conference Series* (Vol. 4, No. 1, pp. 215-249). The Geological Society of London.
- Reedy, C. L. (1994). Thin-section petrography in studies of cultural materials. *Journal of the American Institute for Conservation*, 33(2), 115-129.
- Rigby, S. P., & Alsayah, A. (2023). Storage Sites for Carbon Dioxide in the North Sea and Their Particular Characteristics. *Energies*, 17(1), 211.
- Robertson, B., Buijze, L., Boever, E., & Soustelle, V. (2020). Reservoir characterization of fluvial facies using outcrop and subsurface data: An example from the Lower Triassic Buntsandstein of the Netherlands. *Marine and Petroleum Geology*, 111, 102456.
- Rosenfeld, D., Zhu, Y., Wang, M., Zheng, Y., Goren, T., & Yu, S. (2021). Mining subpixel geological information from hyper-spectral remote sensing imagery: Methodology and application. *Remote Sensing of Environment*, 266, 112694.
- Ruffell, A., & Worden, R. H. (2004). Integration of diagenesis, sedimentology, and sequence stratigraphy: concepts for prediction of reservoir quality in siliciclastic sedimentary rocks. *AAPG bulletin*, 88(6), 727-748.
- Seemann, U. (1979). Diagenetically formed interstitial clay minerals as a factor in Rotliegend sandstone reservoir quality in the Dutch sector of the North Sea. *Journal of Petroleum Geology*, 1(3), 55-62.
- Schmidt, V., Ghanbari, E., & Aarnes, I. (2019). The mineralogical effect of low salinity water-flooding on sandstone diagenesis. *Arabian Journal of Geosciences*, 12(6), 203.
- Schuurman, F., Overeem, I., de Boer, P. L., & De Haas, T. (2020). Facies architecture and depositional evolution of a Late Pleistocene meandering river in the North Sea: Insights from 3D seismic data. *Marine and Petroleum Geology*, 120, 104554.
- Smith, M. J., Worden, R. H., & Bottrell, S. H. (2002). Carbon and oxygen isotope constraints on the origin and thermal history of Rotliegend mineralization in the Southern Permian Basin, UK. *Journal of the Geological Society*, 159(3), 253-265.

- Söllner, F., & Kukla, P. A. (2019). An integrated sedimentology and diagenesis study in Rotliegend sandstones of the NE Dutch offshore. *Marine and Petroleum Geology*, 104, 432-449.
- Tanner, D. C. (1999). Interpretation of Rotliegend sediment provenance from garnet geochemistry. Geological Society, London, Special Publications, 158(1), 191-212.
- Taylor, K. G., & Worden, R. H. (2004). A practical guide to sedimentology and stratigraphy. Edinburgh: Blackwell Science.
- Teuber, L., & Ebbing, J. (2013). Morphometric analysis of seismic geomorphology to quantify the tectonic activity and relative chronology of faulting in the North Sea. *Marine and Petroleum Geology*, 43, 424-440.
- Thorne, J. P., Reading, H. G., & Watney, W. L. (1989). Faulting processes and their implications in siliciclastic rocks. Geological Society, London, Special Publications, 45(1), 115-131.
- Urai, J. L., Spiers, C. J., & Zwart, H. J. (1994). A micromechanical investigation of compaction and dilatancy in porous sandstones. *Journal of the Geological Society*, 151(2), 209-221.
- Van der Laan, J. P., De Bruin, G., Brouwer, F. M., Mijnlief, H. F., Peters, H. H., Rensbergen, P., ... & Van Veen, J. H. (2000). The Jurassic–Cretaceous uplift history of the NE Atlantic continental margin in the Farsund Basin area (southern Norway). *Tectonophysics*, 328(1-2), 1-20.
- Van Dijk, J., Douwe de Jong, C., & Zijp, M. (2009). The first four hydrocarbon prospects in the Netherlands Offshore—Lessons learned from recent exploration drilling in mature basin areas. *Netherlands Journal of Geosciences*, 88(1), 3-16.
- Van Dijk, P. M., & Okkerman, J. (1995). The structural influence on diagenetic changes in Rotliegend reservoir rocks, northern Netherlands. *AAPG bulletin*, 79(7), 1062-1078.
- Van Hulten, F. F. N. (2006, September). Reservoir quality distribution as tool for better exploration prospect evaluation and estimation of the resource base in the Netherlands. In Van Hulten, FFN & Lutgert, JE (comp.). *Tight gas fields in the Netherlands*, workshop EBN-TNO, September (Vol. 19).
- Van Wees, J. D., Staalduinen, C. J., & De Jager, J. (2009). Petroleum systems and hydrocarbon plays of the Netherlands. *AAPG Bulletin*, 93(3), 341-372.
- Worden, R. H., & Morad, S. (2003). Clay minerals in sandstones: controls on formation, distribution and evolution. *AAPG bulletin*, 87(4), 495-508.
- Worden, R. H., & Morad, S. (2000). Quartz cementation in sandstones: a review. *AAPG bulletin*, 84(6), 817-838.
- Wright, V. P. (1992). Rapid transformation of porewaters in relation to late diagenetic mineral growth in sedimentary basins: An overview. *Sedimentary Geology*, 80(1-2), 143-156.
- Zeng, X., & Finkelman, R. B. (2016). Petrology and geochemistry of the Chiling-Kalimash Coal-field, Xinjiang Province, China. *International Journal of Coal Geology*, 154, 194-208.

Zhang, J., & Wang, G. (2014). Fault geometry, segmentation and kinematic evolution of the South China Sea: Insights from dense wide-angle seismic data. *Marine and Petroleum Geology*, 58, 616-632.

10 Appendix

Thin Section	Dolomite (vein)	Dolomite (cement)	Clay (vein)	Clay (cement)	Kaolinite (vein)	Kaolinite (cement)	Illite (vein)	Illite (cement)	Quartz	Feldspar	Lithic Grain	Bitumen	Heavy Minerals	Primary Porosity	Fracture Porosity	Vuggy Porosity	Total
1	0.0	2.4	0.0	10.8	4.4	0.0	0.0	0.4	68.4	0.0	3.6	4.8	0.0	5.2	0.0	0.0	100.0
2	0.0	12.4	0.0	8.4	2.0	0.0	0.0	0.0	64.8	0.0	5.2	4.8	0.4	2.0	0.0	0.0	100.0
3	0.0	4.0	14.0	12.8	4.0	0.4	0.0	0.0	59.6	0.0	3.2	0.0	0.4	1.6	0.0	0.0	100.0
4	1.6	5.8	7.6	8.4	2.0	0.0	0.0	0.4	66.4	0.0	2.8	2.0	0.0	3.6	0.0	0.0	100.0
5	9.6	2.8	5.2	6.0	2.4	8.8	0.0	0.0	56.4	0.0	4.4	0.8	0.0	1.2	2.4	0.0	100.0
6	14.4	10.4	5.2	1.6	2.0	2.4	0.0	0.0	56.4	0.0	2.8	2.0	0.0	2.8	0.0	0.0	100.0
7	0.0	5.6	0.0	6.4	11.2	0.0	0.0	0.0	63.2	0.0	0.8	12.4	0.0	0.0	0.4	0.0	100.0
8	0.0	9.2	0.0	12.8	4.0	0.0	0.0	0.0	66.0	0.0	2.0	2.4	0.4	2.8	0.0	0.4	100.0
9	0.0	8.4	0.8	8.8	2.4	0.0	0.0	0.0	70.4	0.0	2.4	1.2	0.8	4.8	0.0	0.0	100.0
10	6.0	2.8	0.0	4.4	1.2	0.0	0.0	0.0	71.2	0.0	2.8	4.4	0.0	7.2	0.0	0.0	100.0

11	5.2	5.2	0.4	3.2	0.8	1.6	0.0	0.0	72.4	0.0	1.2	0.0	0.0	9.6	0.4	0.0	100 .0
----	-----	-----	-----	-----	-----	-----	-----	-----	------	-----	-----	-----	-----	-----	-----	-----	-----------

Table 1: Results (in percentages) of the petrographic analysis on the thin sections from the K06-04 core.



Figure 1: Grapical representation of the percentages determined during the point counting analysis.

10.1 Ferrous Drop

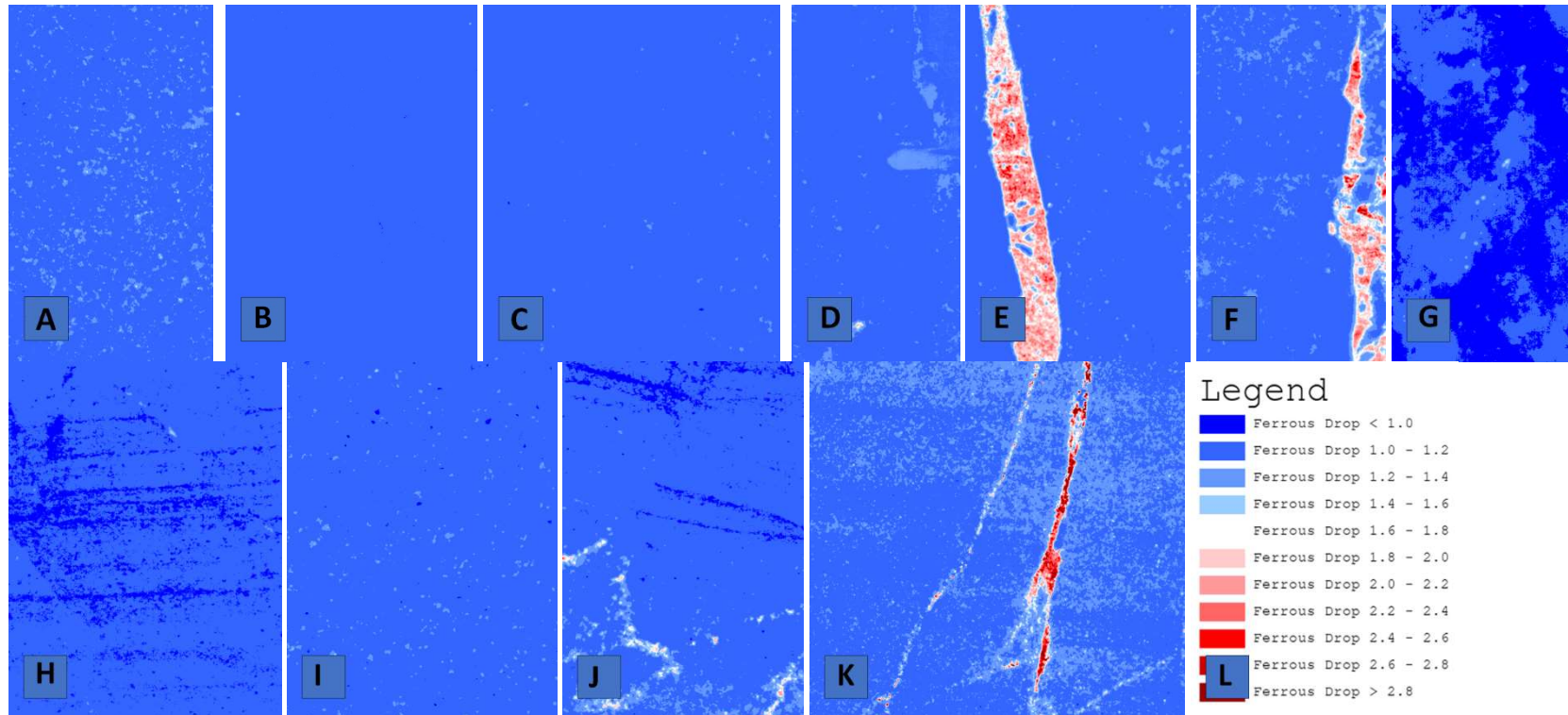


Figure 2: Iron drop values for all the scanned samples (letters A-K correspond to thin section and samples numbers 1-11 respectively).

10.2 Illite crystallinity

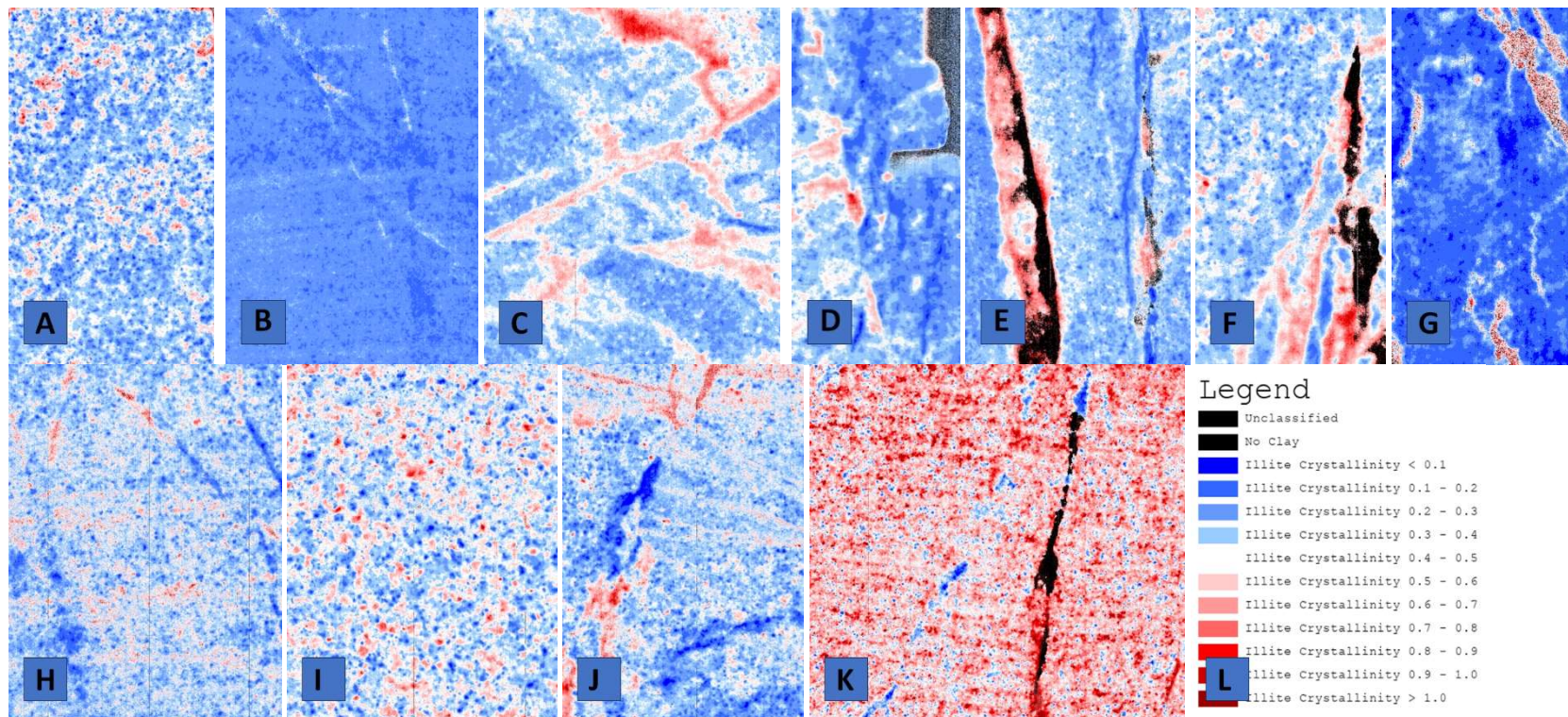


Figure 3: Illite crystallinity values for all the scanned samples (letters A-K correspond to thin section and samples numbers 1-11 respectively).

10.3 Illite vs kaolinite

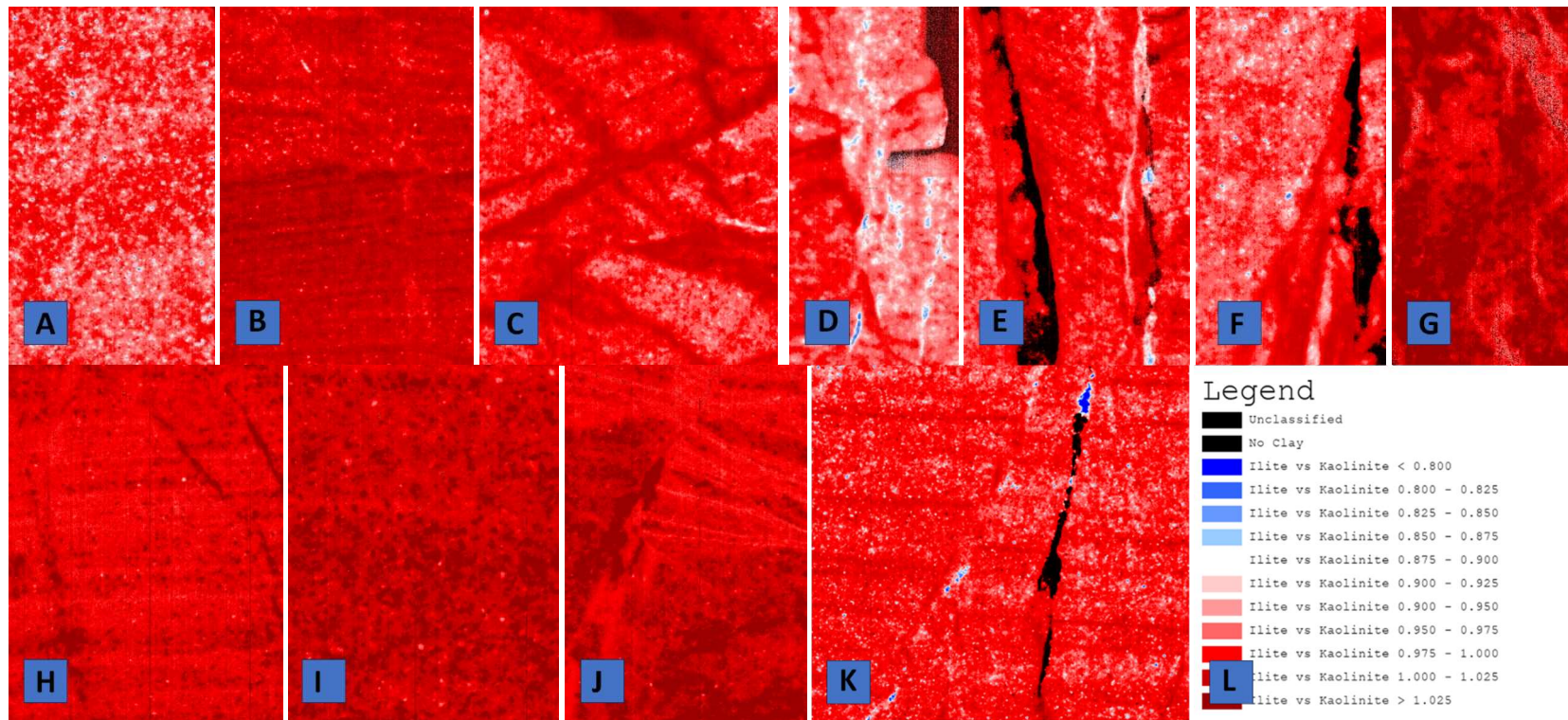


Figure 4: Illite vs Kaolinite values for all the scanned samples (letters A-K correspond to thin section and samples numbers 1-11 respectively).

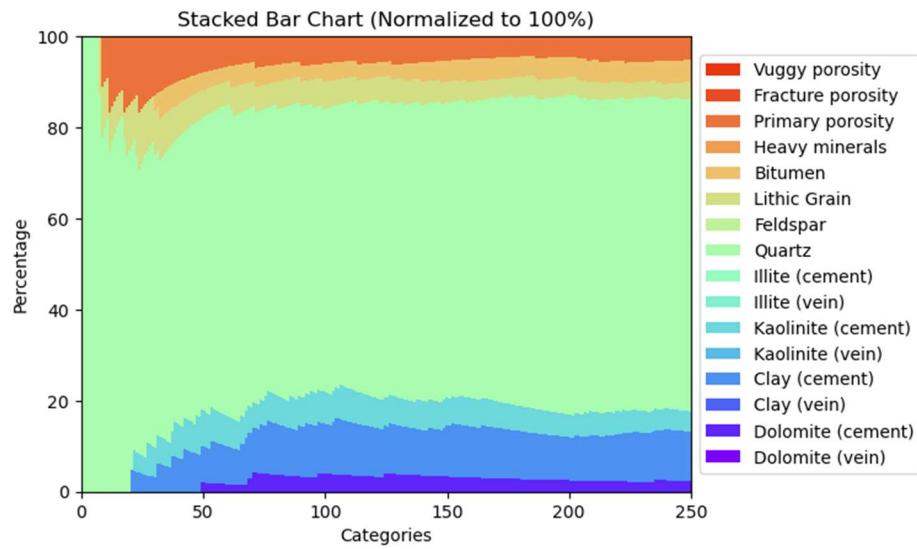


Figure 5: Stack bar chart of thin section 1. The trend of the different counted components appears to stabilize as more components are counted.

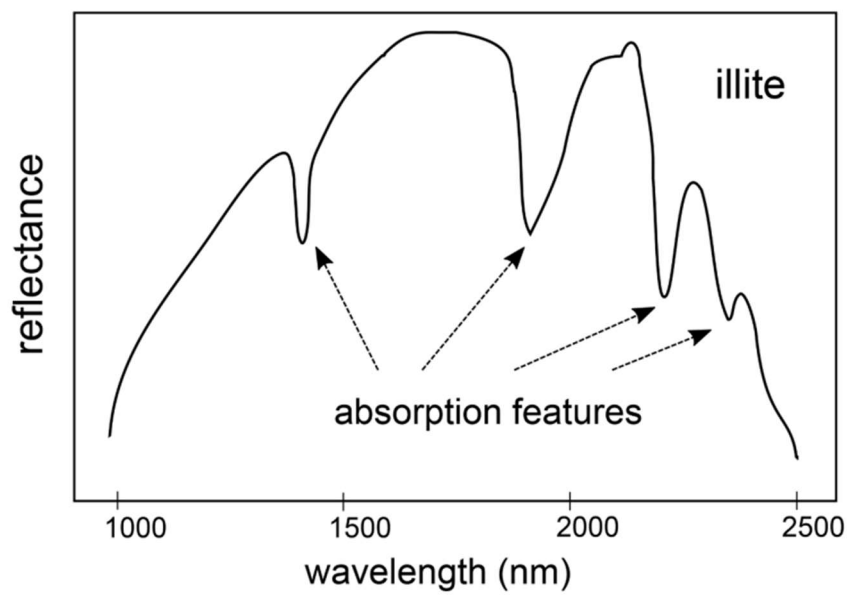


Figure 6: SWIR spectrum that shows different absorption features. For the wavelength maps, the three deepest of these in a specific range are chosen. Image from Savitri et al. 2021.